A coupled implicit MPM-FEM approach for brittle fracture and fragmentation

Ahmad Chihadeh[a], William Coombs[b], Michael Kaliske[a,*]

[a]*Institute for Structural Analysis, Technische Universität Dresden, 01062 Dresden, Germany*
[b]*School of Engineering and Computing Sciences, Durham University, South Road, Durham DH1 3LE, United Kingdom*

Abstract

A new approach has been developed that couples the Material Point Method (MPM) with the Finite Element Method (FEM). The introduced coupling method is achieved by utilizing a bond element to connect the material points to the finite elements, and employing the penalty approach to prevent slippage. Moreover, the developed approach deals with the contact between MPM and FEM. The contact is regulated by introducing additional conditions. When these conditions are met, the bond elements become active and prevent penetration. The coupling is monolithic, meaning that one system of equations is built for both MPM and FEM, and solved simultaneously. Additionally, an automated conversion of finite elements to material points is presented, which is controlled by the eigenfracture approach that splits the finite elements into intact and eroded sets. Eroded finite elements are then converted to material points. Numerical examples are reported to express the novelty of the developed approach.

Keywords: Material Point Method, Finite Element Method, Eigenfracture, Fracture, Large deformation, Coupling MPM-FEM

*Corresponding author
Email address: michael.kaliske@tu-dresden.de (Michael Kaliske)

1. Introduction

The Material Point Method (MPM), introduced by Sulsky *et al.* [36], is applied in problems where extreme deformations are addressed, especially when the material being analysed includes a stress history dependence. The MPM is a hybrid method which consists of particles that represent the simulated specimen, and a background computational mesh where the weak formulation of the problem is solved. Every time step, the data are exchanged between the particles, called material points, and the background mesh. Within a time step, the data are mapped to the mesh, the unknown field is evaluated, the result mapped back to the material points, and, the computational mesh is reset to the undeformed shape which is the main reason why the MPM is a good choice to be used for problems with extreme deformations.

Most of the MPM applications available in the literature address an explicit time integration scheme. On the other side, few efforts have been made to consider an implicit formulation [5, 7, 8, 9, 14]. In this work, the implicit framework is addressed. Compared to the explicit time integration scheme, in the implicit scheme, a bigger time step can be applied, without degrading the accuracy of the computed result.

Due to its hybrid nature, the MPM can overcome the problem of large element distortion that Finite Element Method (FEM) has as a shortcoming. On the other side, the MPM has also some disadvantages. Compared to the FEM, the MPM consumes more computational time, it is less accurate, and it has less numerical stability. Hence, the simulation can be optimized if the two methods are coupled and applied at the same time, in a way that the MPM is only applied in the field where the deformations are extremely large, and the FEM is applied elsewhere. This description is summarized as coupling MPM-FEM, which is the topic of this paper at hand. Coupling MPM and FEM has not been studied much in the literature. Few studies are available. In [2], the coupling is limited to finite elements undergoing small displacements, and the whole computational grid is involved in the problem solution, even the inactive nodes. [6, 17, 18] work on the explicit time integration scheme, and, in [7], the coupling is presented for truss finite elements only.

An implicit monolithic coupling of MPM and FEM is introduced in this research. The coupling is achieved by bond elements located at the interface between the material points and the finite elements. The bond elements connect the finite elements to the active elements in the background mesh of the MPM. One single system of equations is built and the solution for the MPM part and the FEM part is calculated simultaneously. A penalty approach is applied in the bond element in order to prevent a slip between the finite elements and the material points, or more precisely the activated elements of the MPM.

Contact between material points and finite elements is also introduced in this work. The contact is implemented using the same bond element formulation. However, additional conditions are applied in order to activate and deactivate the contact bond elements. The two bodies have to be close enough, as the activated elements can extend beyond the physical surface of the body, and they have to be approaching each other.

As a further step to enhance the predictive capabilities of the method, a conversion of finite elements to material points is applied during the simulation. In this way, a minimum number of material points shall be used, and only the finite elements which are determined based on certain criteria will be replaced by material points. This approach removes the task of defining which domain is discretized by MPM and which is discretized by FEM prior to the simulation. This description is introduced in this paper at hand as an automated conversion of finite elements to material points. One or more criteria can be defined to control the conversion, depending on the nature of the problem being simulated. For instance, the criterion could be the degree of element distortion or the damage percentage. In this study, the eigenfracture approach [23] serves as a criterion for the conversion. It is a fracture model which defines a crack as a set of eroded elements. Hence, in the introduced approach, the eroded finite elements are converted to material points.

Many versions of the MPM have been introduced. Mainly to mitigate the so-called cell crossing noise, which arises when the material points cross element boundaries of the computational mesh. The Generalized Interpolation Material Point (GIMP) method [3], the Convected Particle Domain Interpolation (CPDI) method [26], the second order Convected Particle Domain Interpolation (CPDI2) method [22, 27], Dual Domain Material Point

(DDMP) method [11, 19, 40], and in addition to applying B-spline shape functions [13, 37, 39]. CPDI2 is the adopted version of MPM for the coupling introduced in this paper. It is necessary to maintain the connection between the finite element boundaries and the material point domain boundaries. This can only be achieved by the CPDI2 method.

The article is organized as follows. In Section 2, the basics and the formulations of the implicit MPM are shown in addition to a brief description of the CPDI2 approach. Section 3 explains the coupling method developed in this work. The automated conversion of finite elements to material points is introduced in Section 4. Numerical examples are shown and discussed in Section 5. Finally, conclusive remarks are given in Section 6.

2. Implicit MPM

The formulation of the MPM is similar to the formulation of the FEM. One can think about the MPM as an FEM with moving Gauss points, as the material points play the same role as the Gauss points do in the FEM [14]. However, the material points move over a computational mesh and carry all the relevant information for the computation. Each time step consists of three phases. The first phase is mapping body forces, external forces, mass, momentum, and inertia from the material points to the nodes which is achieved by

$$\square_v = \sum_{p=1}^{np} \boldsymbol{N}(\boldsymbol{\xi}_p)^T \square_p \ , \tag{1}$$

where the subscripts v and p indicate nodes and material points, respectively, $\boldsymbol{N}$ is the matrix of the shape functions, $\boldsymbol{\xi}_p$ is the local coordinate of material point p, and np is the number of material points in the element. $\square$ are the mapped data. The second phase is solving for the unknown nodal displacements, which in general are solved by an iterative process

$$\begin{aligned} \boldsymbol{K}^i \Delta \boldsymbol{u}_v &= \boldsymbol{f}^i \ , \\ \boldsymbol{u}_v^{i+1} &= \boldsymbol{u}_v^i + \Delta \boldsymbol{u}_v \ , \end{aligned} \tag{2}$$

where $\boldsymbol{K}$ is the stiffness matrix, $\boldsymbol{u}_v$ and $\Delta \boldsymbol{u}_v$ are the nodal displacement and displacement increment vectors, respectively, $\boldsymbol{f}$ is the residual vector, and the superscript is the iteration number. The third phase then is mapping

displacements and acceleration from the nodes to the material points, which is achieved by

$$\square_p = \boldsymbol{N}(\boldsymbol{\xi}_p)\ \square_v\ , \tag{3}$$

and resetting the computational mesh to the undeformed configuration.

2.1. Formulation of non-linear implicit MPM

As mentioned above, the MPM is an FEM with moving Gauss points, the mathematical formulations are the same. The only difference is that the material points are used to evaluate the numerical integration instead of the Gauss points (integration points) in the FEM. Hence the discretized weak form of the equilibrium is given by

$$\int_V \boldsymbol{N}^T \rho \boldsymbol{N}\ \ddot{\boldsymbol{u}}_v \,\mathrm{d}V + \int_V \boldsymbol{B}^T\ \boldsymbol{\sigma}\,\mathrm{d}V = \int_V \boldsymbol{N}^T\ \boldsymbol{b}\,\mathrm{d}V + \int_A \boldsymbol{N}^T\ \boldsymbol{t}\,\mathrm{d}A\ , \tag{4}$$

where ρ is the material density, $\ddot{\boldsymbol{u}}_v$ is the nodal acceleration vector, $\boldsymbol{B}$ is the matrix of shape function derivatives, $\boldsymbol{\sigma}$ is the Cauchy stress, body forces $\boldsymbol{b}$ acting over the volume V, A is the domain surface, and $\boldsymbol{t}$ is the applied traction [4, 10]. In this paper, geometrical non-linearity is included and the St. Venant-Kirchhoff material model is applied. Hence, Eq. (4) is non-linear in terms of the nodal displacements. Applying the implicit Newmark scheme for time discretization and using the Newton-Raphson method for solving nonlinear problems, after linearisation, the vector of internal forces and the stiffness matrix of a material point are given by

$$\boldsymbol{f}_p = \boldsymbol{B}_L^T \boldsymbol{\sigma}\ V_p\ , \tag{5}$$

$$\boldsymbol{K}_p^* = \frac{1}{\beta \Delta t^2}\boldsymbol{M}_p + \boldsymbol{K}_p\ , \tag{6}$$

where β is the Newmark parameter, Δt is the time step, $\boldsymbol{M}_p$ is the mass matrix, and the tangential stiffness matrix $\boldsymbol{K}_p$ is given by

$$\boldsymbol{K}_p = \left[\boldsymbol{B}_L^T \cdot \boldsymbol{C}_T \cdot \boldsymbol{B}_L + \boldsymbol{B}_{NL}^T \cdot \boldsymbol{\sigma} \cdot \boldsymbol{B}_{NL}\right] V_p\ , \tag{7}$$

where $\boldsymbol{C}_T$ is the tangential material tensor, V_p is the material point volume, and $\boldsymbol{B}_L$ and $\boldsymbol{B}_{NL}$ are matrices of the shape function derivatives that have

the form in the general three-dimensional case

$$\boldsymbol{B}_L = \begin{bmatrix} N_{1,x} & 0 & 0 & ... & N_{n,x} & 0 & 0 \\ 0 & N_{1,y} & 0 & ... & 0 & N_{n,y} & 0 \\ 0 & 0 & N_{1,z} & ... & 0 & 0 & N_{n,z} \\ 0 & N_{1,z} & N_{1,y} & ... & 0 & N_{n,z} & N_{n,y} \\ N_{1,z} & 0 & N_{1,x} & ... & N_{n,z} & 0 & N_{n,x} \\ N_{1,y} & N_{1,x} & 0 & ... & N_{n,y} & N_{n,x} & 0 \end{bmatrix}, \tag{8a}$$

$$\boldsymbol{B}_{NL} = \begin{bmatrix} N_{1,x} & 0 & 0 & ... & N_{n,x} & 0 & 0 \\ N_{1,y} & 0 & 0 & ... & N_{n,y} & 0 & 0 \\ N_{1,z} & 0 & 0 & ... & N_{n,z} & 0 & 0 \\ 0 & N_{1,x} & 0 & ... & 0 & N_{n,x} & 0 \\ 0 & N_{1,y} & 0 & ... & 0 & N_{n,y} & 0 \\ 0 & N_{1,z} & 0 & ... & 0 & N_{n,z} & 0 \\ 0 & 0 & N_{1,x} & ... & 0 & 0 & N_{n,x} \\ 0 & 0 & N_{1,y} & ... & 0 & 0 & N_{n,y} \\ 0 & 0 & N_{1,z} & ... & 0 & 0 & N_{n,z} \end{bmatrix}, \tag{8b}$$

respectively, where $N_{n,i}$ is the derivative of shape function at node n with respect to i, with $i = \{x, y, z\}$.

The standard MPM suffers from the so-called cell crossing noise. This problem happens when the material points cross element boundaries, causing numerical oscillation and incorrect stress values. More explanation is provided in [8]. In order to mitigate the problem, different versions of MPM have been introduced. For instance, the Generalized Interpolation Material Point (GIMP) method [3], the Convected Particle Domain Interpolation (CPDI) [26], and the second order Convected Particle Domain Interpolation (CPDI2) [22, 27]. In this paper, the CPDI2 is used which is briefly explained in the following section.

2.2. Second order Convected Particle Domain Interpolation (CPDI2)

In the CPDI2, particle domains are tracked as quadrilaterals in 2D and hexahedra in 3D. The CPDI is a development out of the GIMP. In the GIMP, the simplified weighting and gradient weighting functions, with a piecewise constant particle characteristic function, are given by

$$
\begin{aligned}
S_{vp} &= \frac{1}{V_p}\int_{\Omega_p} N_v(x)d\Omega \ , \\
\nabla S_{vp} &= \frac{1}{V_p}\int_{\Omega_p} \nabla N_v(x)d\Omega \ ,
\end{aligned}
\tag{9}
$$

where Ω_p is the influence domain of the material point, Ω is the problem domain, N_v is the shape function of the background finite element grid. In the CDPI2, the shape function is replaced by an alternative function [22] given by

$$
N_v^{alt}(x) = \sum_{c=1}^{nc} M_c(x) N_v(x_c) \ , \tag{10}
$$

where $M_c(x)$ are the shape functions of quadrilateral elements in 2D and hexahedral elements in 3D, nc is 4 and 8 in 2D and 3D, respectively, and $N_v(x_c)$ are the shape functions of the computational mesh evaluated at the domain corners. Eq. (9) becomes

$$
\begin{aligned}
S_{vp} &= \frac{1}{V_p}\int_{\Omega_p} N_v^{alt}(x)d\Omega = \frac{1}{V_p}\int_{\Omega_p}\left[\sum_{c=1}^{nc} M_c(x)N_v(x_c)\right]d\Omega \\
&= \frac{1}{V_p}\sum_{c=1}^{nc}\left[\int_{\Omega_p} M_c(x)d\Omega\right] N_v(x_c) \ , \\
\nabla S_{vp} &= \frac{1}{V_p}\int_{\Omega_p} \nabla N_v^{alt}(x)d\Omega = \frac{1}{V_p}\int_{\Omega_p}\left[\sum_{c=1}^{nc} \nabla M_c(x)N_v(x_c)\right]d\Omega \\
&= \frac{1}{V_p}\sum_{c=1}^{nc}\left[\int_{\Omega_p} \nabla M_c(x)d\Omega\right] N_v(x_c) \ .
\end{aligned}
\tag{11}
$$

Nguyen *et al.* [22] derive the solution of the integrals in the square brackets for 2D bilinear quadrilateral element, which is used in this paper. The integrals for the hexahedral element in 3D are evaluated numerically.
The main reason, why the CPDI2 is used in this work, is the coupling with the FEM. It is necessary to update the displacements of the domain corners exactly as the mesh is deformed. In the next section, the coupling with the FEM is introduced.

3. Coupling MPM with FEM

The FEM, compared to the MPM, is faster, more accurate, and numerically more stable. Accordingly, it is more efficient to use the MPM only in the parts of the domain where the FEM will fail. In this paper, a monolithic coupling of the implicit MPM with the FEM is introduced. The coupling is achieved by introducing bond elements which connect the finite elements to the activated elements in the computational mesh of the MPM. The bond elements are applied at the common boundaries of the finite elements with the material points.

3.1. Nodal bond elements

In order to describe the nodal bond element, a simple structure is considered as shown in Fig. 1. The left half is discretized by the MPM and the right one by the FEM. Fig. 1 shows the different components of the MPM and the FEM.

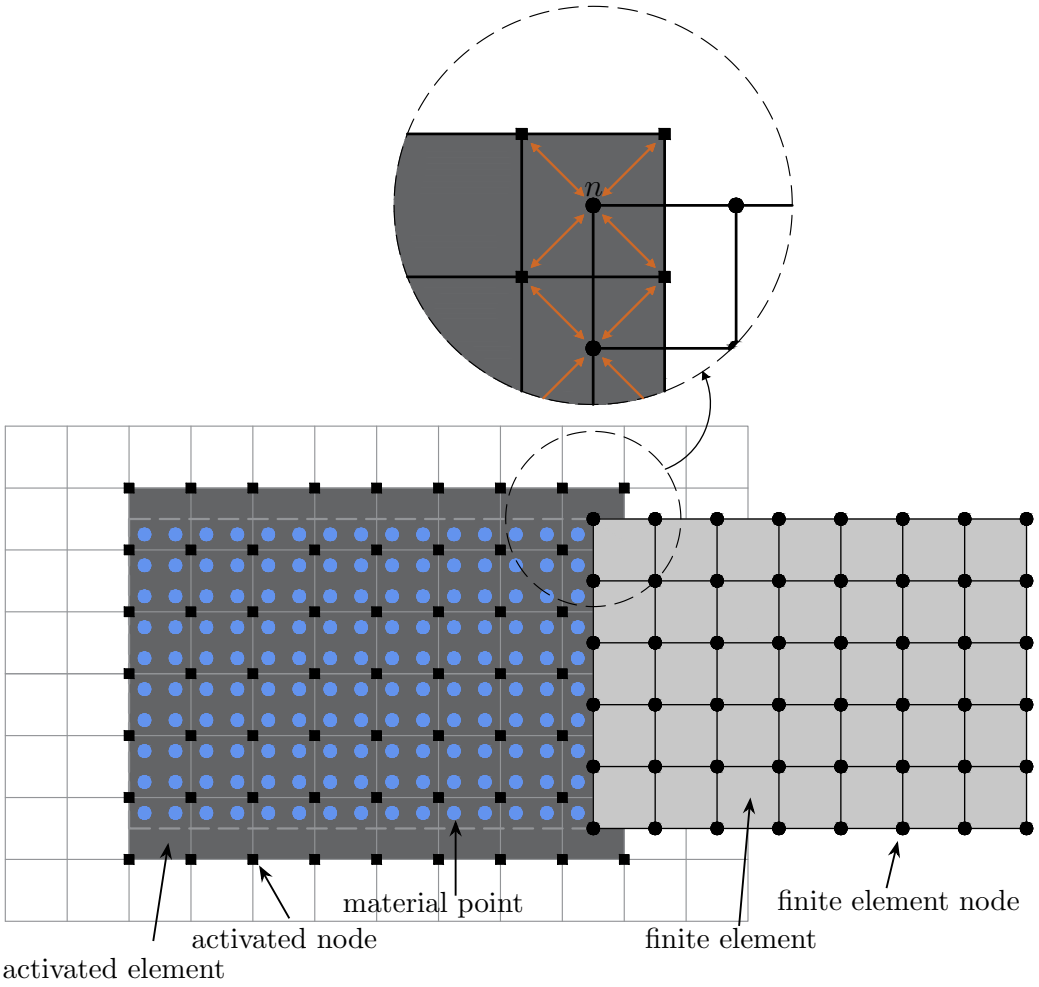

Figure 1: Coupling components of MPM with FEM.

The nodal bond element is represented by the arrows connecting the finite element node n to the nodes of the activated element in the background mesh. At each node of the finite elements with common boundary with the material points, a nodal bond element is created. Theoretically, the displacement of the finite element node n and the displacement at the same location of the activated element should be the same. Hence the displacement slip vector $\boldsymbol{s}$ should be kept equal to zero, which is given by

$$\boldsymbol{s} = \boldsymbol{u}_n - \boldsymbol{u}_{nc} \ , \tag{12}$$

with

$$\boldsymbol{u}_{nc} = \boldsymbol{N}_c(\boldsymbol{\xi}_{nc})\ \boldsymbol{u}_v\ , \tag{13}$$

the slip vector is given by

$$\boldsymbol{s} = [\mathbf{1} - \boldsymbol{N}_c(\boldsymbol{\xi}_{nc})] \left\{ \begin{array}{c} \boldsymbol{u}_n \\ \boldsymbol{u}_v \end{array} \right\} = \boldsymbol{B}_b \left\{ \begin{array}{c} \boldsymbol{u}_n \\ \boldsymbol{u}_v \end{array} \right\}\ , \tag{14}$$

where in the three-dimensional case

$$\mathbf{1} = \left[\begin{array}{ccc} 1 & 0 & 0 \\ 0 & 1 & 0 \\ 0 & 0 & 1 \end{array} \right]\ , \tag{15}$$

and $\boldsymbol{N}_c$ is the shape function matrix of the activated element, which yields for the hexahedral element the form

$$\boldsymbol{N}_c(\boldsymbol{\xi}_{nc}) = \left[\begin{array}{ccccccc} N_1(\boldsymbol{\xi}_{nc}) & 0 & 0 & \cdots & N_8(\boldsymbol{\xi}_{nc}) & 0 & 0 \\ 0 & N_1(\boldsymbol{\xi}_{nc}) & 0 & \cdots & 0 & N_8(\boldsymbol{\xi}_{nc}) & 0 \\ 0 & 0 & N_1(\boldsymbol{\xi}_{nc}) & \cdots & 0 & 0 & N_8(\boldsymbol{\xi}_{nc}) \end{array} \right]\ , \tag{16}$$

and $\boldsymbol{\xi}_{nc}$ is the local coordinates of node n in the activated element, $\boldsymbol{u}_n$ is the displacement of node n, $\boldsymbol{u}_{nc}$ is the displacement of the activated element at the location of node n, and $\boldsymbol{u}_v$ is the nodal displacement vector of the activated element. The slip induces bond stress

$$\boldsymbol{\sigma}_b = \boldsymbol{C}_b \boldsymbol{s}\ , \tag{17}$$

where $\boldsymbol{C}_b$ is the bond element constitutive relation. Eq. (17) is represented in matrix form as

$$\left\{ \begin{array}{c} \sigma_x \\ \sigma_y \\ \sigma_z \end{array} \right\} = \left[\begin{array}{ccc} C_x & 0 & 0 \\ 0 & C_y & 0 \\ 0 & 0 & C_z \end{array} \right] \left\{ \begin{array}{c} s_x \\ s_y \\ s_z \end{array} \right\}\ , \tag{18}$$

and the slip values are kept close to zero by penalty terms given to C_x, C_y, and C_z, which are user defined.

The bond force is introduced, with one part is applied on the activated element and the other part is applied on the finite element node, given by

$$\boldsymbol{f}_b = \left\{ \begin{array}{c} \boldsymbol{f}_{bn} \\ \boldsymbol{f}_{bc} \end{array} \right\} = \boldsymbol{B}_b^T \boldsymbol{\sigma}_b\ , \tag{19}$$

where $\boldsymbol{f}_{bn}$ is the part of the bond force applied on the finite element node, and $\boldsymbol{f}_{bc}$ is applied on the activated element. Introducing the bond stiffness matrix, $\boldsymbol{K}_b$, and considering Eqs. (14, 17), Eq. (19) is expressed as

$$\boldsymbol{f}_b = \boldsymbol{B}_b^T \, \boldsymbol{C}_b \, \boldsymbol{s} = \boldsymbol{B}_b^T \, \boldsymbol{C}_b \, \boldsymbol{B}_b \left\{ \begin{array}{c} \boldsymbol{u}_n \\ \boldsymbol{u}_v \end{array} \right\} = \boldsymbol{K}_b \left\{ \begin{array}{c} \boldsymbol{u}_n \\ \boldsymbol{u}_v \end{array} \right\} . \tag{20}$$

Bond force $\boldsymbol{f}_b$ and bond stiffness $\boldsymbol{K}_b$ are assembled on the system level for each bond element. The coupled monolithic system is given by

$$\left[\begin{array}{cc} \boldsymbol{K}_{MPM+be} & \boldsymbol{K}_{be} \\ \boldsymbol{K}_{be} & \boldsymbol{K}_{FEM+be} \end{array} \right] \left\{ \begin{array}{c} \Delta\boldsymbol{u}_{MPM} \\ \Delta\boldsymbol{u}_{FEM} \end{array} \right\} = \left\{ \begin{array}{c} \boldsymbol{f}_{MPM+be} \\ \boldsymbol{f}_{FEM+be} \end{array} \right\} , \tag{21}$$

where the subscripts indicate the associated contribution. Subscript *be* denotes bond elements.

Fig. 2 shows a 1×5 cm cantilever beam under dynamic loading discretized by MPM, FEM, and MP-FE method. The nodal bond elements are shown in Fig. 2c. The beam is fixed at the left edge and loaded by 8 N at the tip with a triangular loading function $\{(0, 0), (0.1, 1), (0.2, 0)\}$. The material has a Young's modulus of 10^4 N/cm^2 and 0.2 Poisson's ratio. The element size, which is 0.1×0.1 cm, is the same for both MPM and FEM, with 2×2 material points per element. It is shown in Fig. 3 that the displacements at the beam tip for the three methods are the same, which indicates a correct implementation of the nodal bond elements.

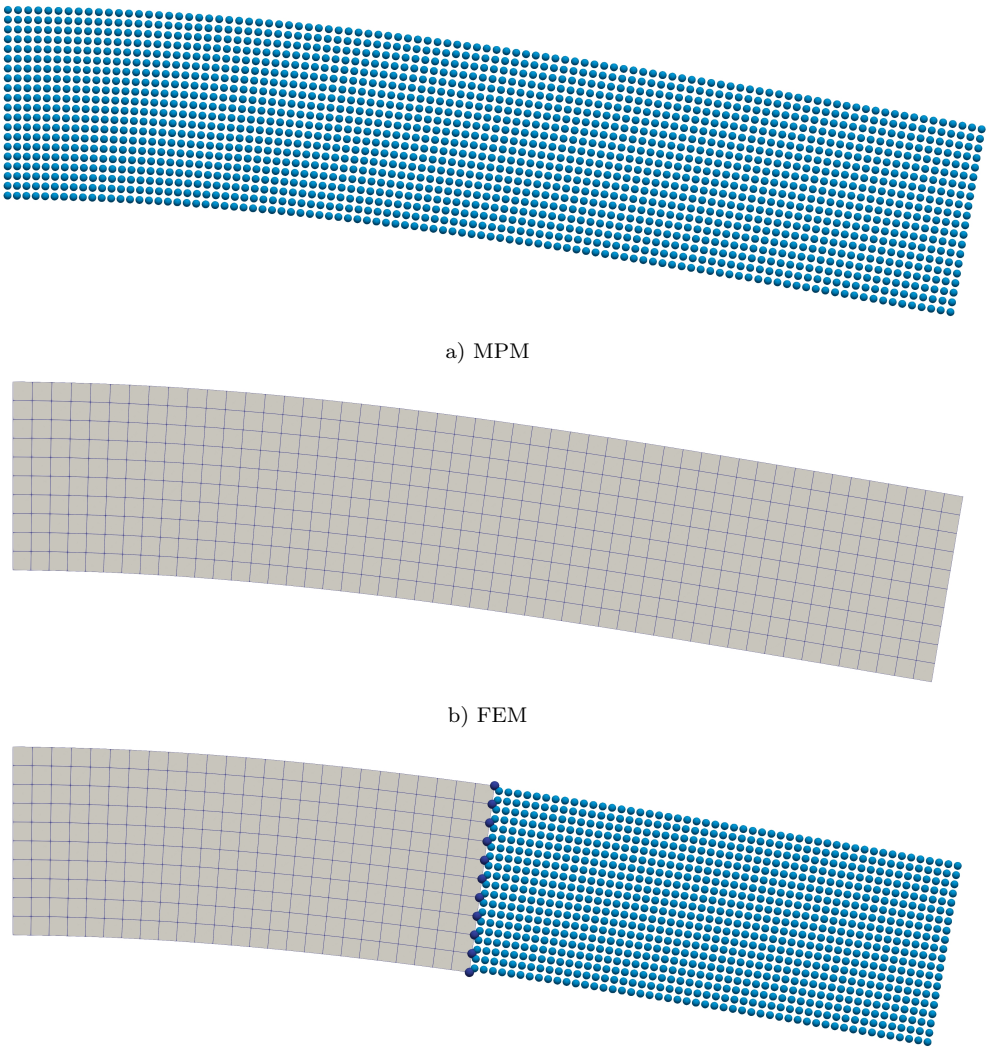

a) MPM

b) FEM

c) MP-FE method

Figure 2: Cantilever beam under dynamic loading discretized by MPM, FEM, and MP-FE method.

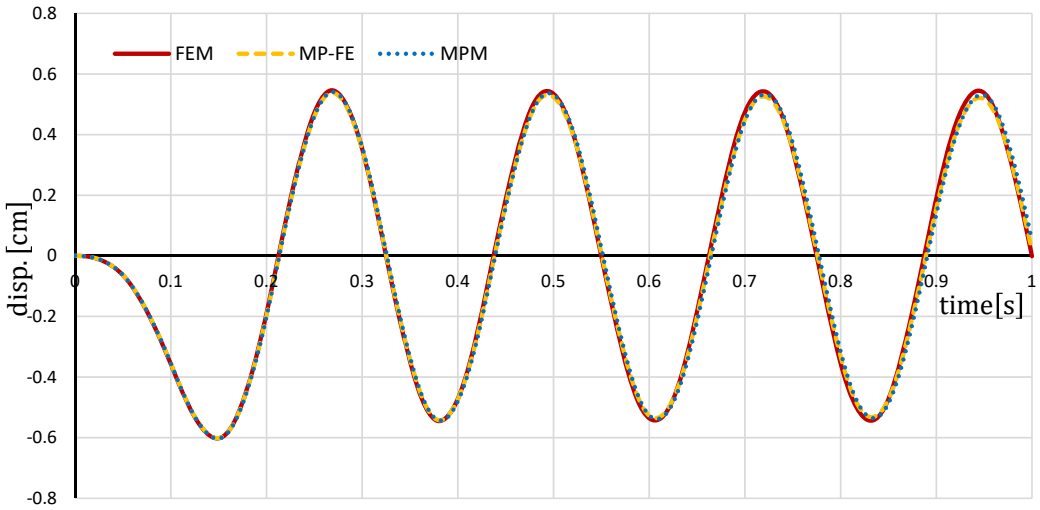

Figure 3: Displacement at cantilever tip.

3.2. Intermediate bond elements

The element size of the FEM and the size of the grid cells in the computational mesh of the MPM do not need to be equal. It is a common trend to use a larger element size in the far field, where not much happens during the simulation. Hence, this study investigates the coupling of MPM and FEM where finite elements have larger element size. Fig. 4a shows a rectangular specimen discretized by MPM and FEM. The specimen is fixed at the left edge and a prescribed displacement is applied at the right edge. Fig. 4b presents the deformed shape, where the element size for both MPM and FEM is the same. Fig. 4c presents the deformed shape where, the element size of the FEM is larger than the element size in the MPM. It is shown that for the case, where the element size is the same, the connectivity between the material points and the finite elements is maintained. However, when the element size is not the same for both, the connectivity is lost and it is only maintained at the location of the finite element nodes, where the nodal bond elements are created.

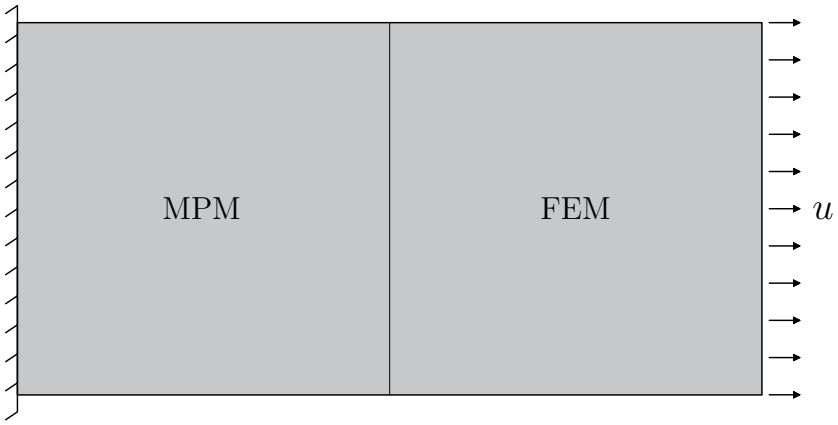

a) Specimen descretized by MPM and FEM under tension

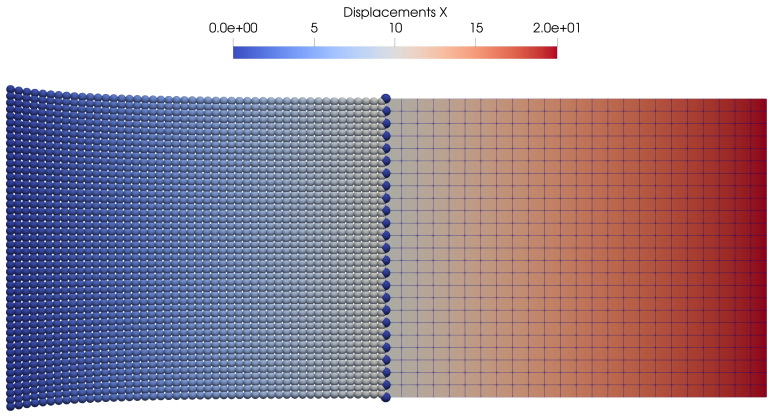

b) Coupling MPM and FEM with equal element size

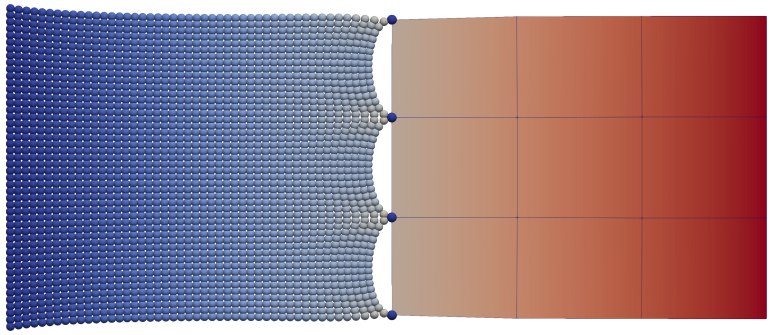

c) Coupling MPM and FEM with larger element size

Figure 4: Response of specimen discretized by coupling MPM and FEM.

Therefore, intermediate bond elements are needed between the finite element nodes. The introduction of the intermediate bond elements is illustrated in Fig. 5. In the same way as the nodal bond elements are formulated, the intermediate bond elements restrain the difference in displacements over the boundary between the FEM and MPM regions. The only difference is that in the intermediate bond elements the displacement of the finite elements is interpolated using the finite element shape functions. As represented by the arrows in Fig. 5, the slip at the intermediate bond element is evaluated by the interpolation of the nodal displacement of the finite element and the nodal displacement of the activated element. The slip is

$$\boldsymbol{s} = \boldsymbol{u}_{ne} - \boldsymbol{u}_{nc} \ , \tag{22}$$

with

$$\boldsymbol{u}_{ne} = \boldsymbol{N}_e(\boldsymbol{\xi}_{ne}) \ \boldsymbol{u}_i \ , \tag{23}$$

and $\boldsymbol{u}_{nc}$ as given in Eq. (13), the slip vector is given by

$$\boldsymbol{s} = [\boldsymbol{N}_e(\boldsymbol{\xi}_{ne}) - \boldsymbol{N}_c(\boldsymbol{\xi}_{nc})] \left\{ \begin{array}{c} \boldsymbol{u}_i \\ \boldsymbol{u}_v \end{array} \right\} = \boldsymbol{B}_b \left\{ \begin{array}{c} \boldsymbol{u}_i \\ \boldsymbol{u}_v \end{array} \right\} \ , \tag{24}$$

where $\boldsymbol{u}_{ne}$ is the finite element nodal displacement, $\boldsymbol{N}_e$ is the matrix of the shape functions of the finite element, $\boldsymbol{\xi}_{ne}$ is the local coordinates of the intermediate bond element in the finite element, and $\boldsymbol{u}_i$ is the finite element displacement vector. Then, the bond force vector and the bond stiffness matrix are formulated in the same way as for the nodal bond element.

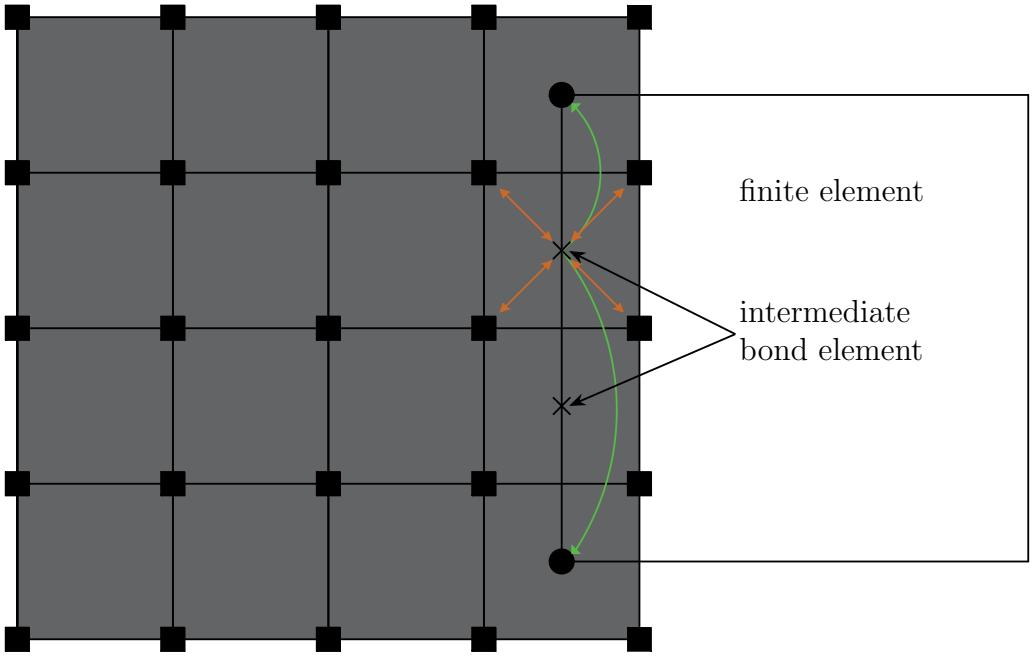

Figure 5: Intermediate bond element.

The same problem shown in Fig. 4a is now simulated with intermediate bond elements included. The deformed shape is shown in Fig. 6. The nodal bond elements are shown in blue and the intermediate bond elements are shown in red. As depicted, the connectivity between the MPM and the FEM with a coarser mesh is maintained.
The coupling, where the finite elements have smaller element size, is not explicity investigated, because the nodal bond elements are created at the finite element nodes, which in this case are more dense than the nodes of the computational grid of the MPM, which means that the connectivity will be maintained. This is in addition to the fact that in practice, the MPM mesh should always be finer than the finite element mesh or at least not coarser, as there large deformations are expected.

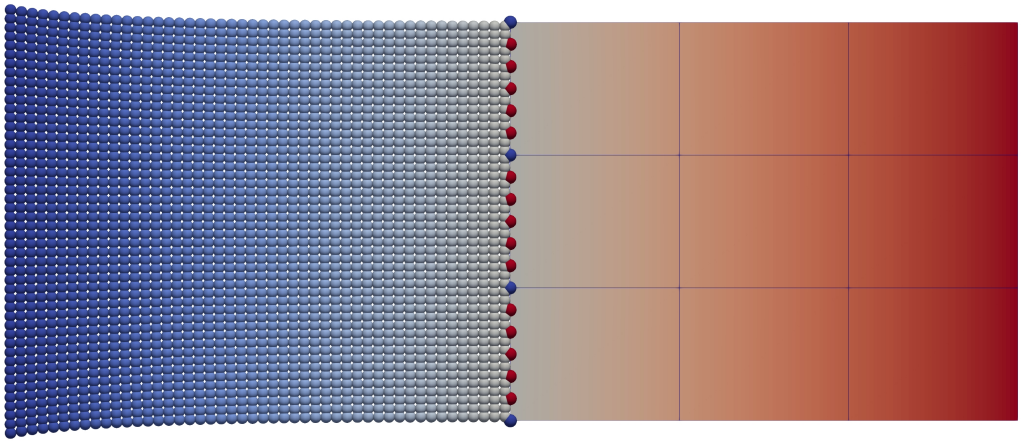

Figure 6: Response of the specimen with intermediate bond elements included.

3.3. Contact of MPM and FEM

The contact of two bodies, one modeled by the MPM and the other by the FEM, is also introduced in this work. The contact is described through the bond elements explained in the previous sections with additional steps in order to check whether the two bodies are in contact. As far as there is not any finite element nodes in any activated element of the computational mesh of the MPM, then the contact does not exist. Once at least one finite element node is inside an activated element, two additional checks are made. The first one is the so-called proximity condition, which is satisfied if

$$d \leq 0 \ , \tag{25}$$

where d is the distance between the surface of the body modeled by the MPM and the finite element node as described in Fig. 7b. If Eq. (25) is satisfied, then the two bodies are checked if they are approaching or separating. The two bodies are approaching if

$$(\boldsymbol{u}_n - \boldsymbol{u}_{nc}) \cdot \boldsymbol{n} > 0 \ , \tag{26}$$

where $\boldsymbol{n}$ is the outward normal vector of the finite element as described in Fig. 7a. If the two conditions are satisfied, then the contact bond element is activated.

The bond element constitutive relation introduced in Eqs. (17, 18) is modified for the contact bond element as follows

$$\boldsymbol{C}_b = \begin{bmatrix} C_n & 0 & 0 \\ 0 & C_t & 0 \\ 0 & 0 & C_t \end{bmatrix} , \tag{27}$$

where C_n and C_t are the constitutive coefficients in the normal and the tangential directions, respectively. Penetration is avoided by a penalty term assigned to C_n. C_t describes the friction between the bodies. In this work, no friction is assumed as $C_t = 0$.

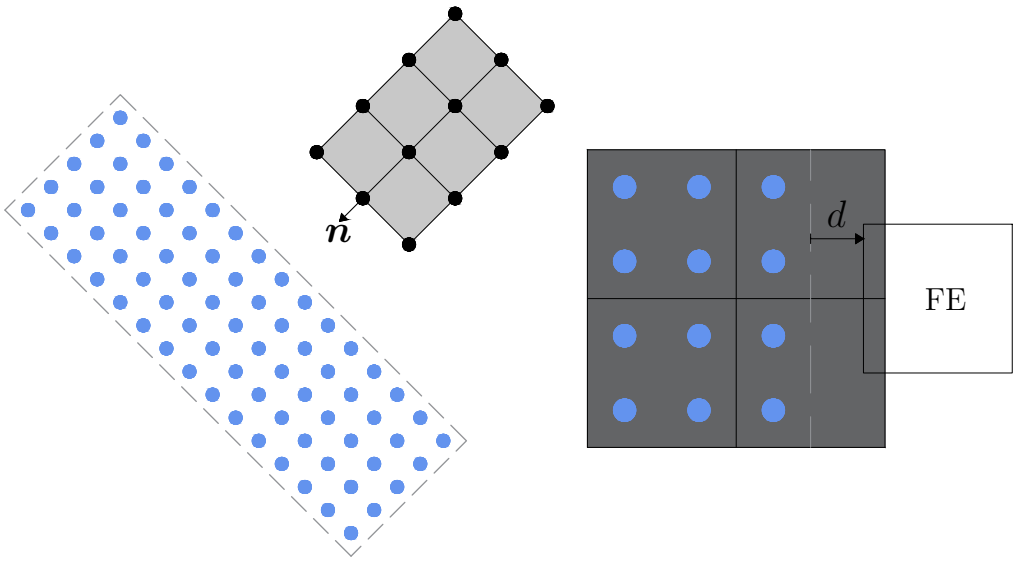

a) Outward normal vector n b) Proximity condition

Figure 7: Contact of MPM and FEM.

A 3D simulation of the MPM-FEM contact problem is presented in Fig. 8. The two types of coupling are included in this simulation, the coupling where the material points and the finite elements are in the same body, and the contact coupling. As shown in Fig. 8, a 3D square frame is discretized by both MPM and FEM, with a small block modeled by FEM inside the frame. The block starts moving with an initial velocity ($v_x = -10$, $v_y = 0$, $v_z = -10$) m/s. The time step is 0.001 s, and the Newmark parameters are $\beta = 0.5$ and $\gamma = 0.5$. The outer dimension of the frame is 11 m and the thickness is 1 m. The depth is 3 m, and it is fixed along the outer corners. The moving block is 1 m cube and the initial location of its center is (5.5,

1.5, 9.5). The material is characterized by a Young's modulus of $E = 10$ GPa and a Poisson's ratio of 0.2.

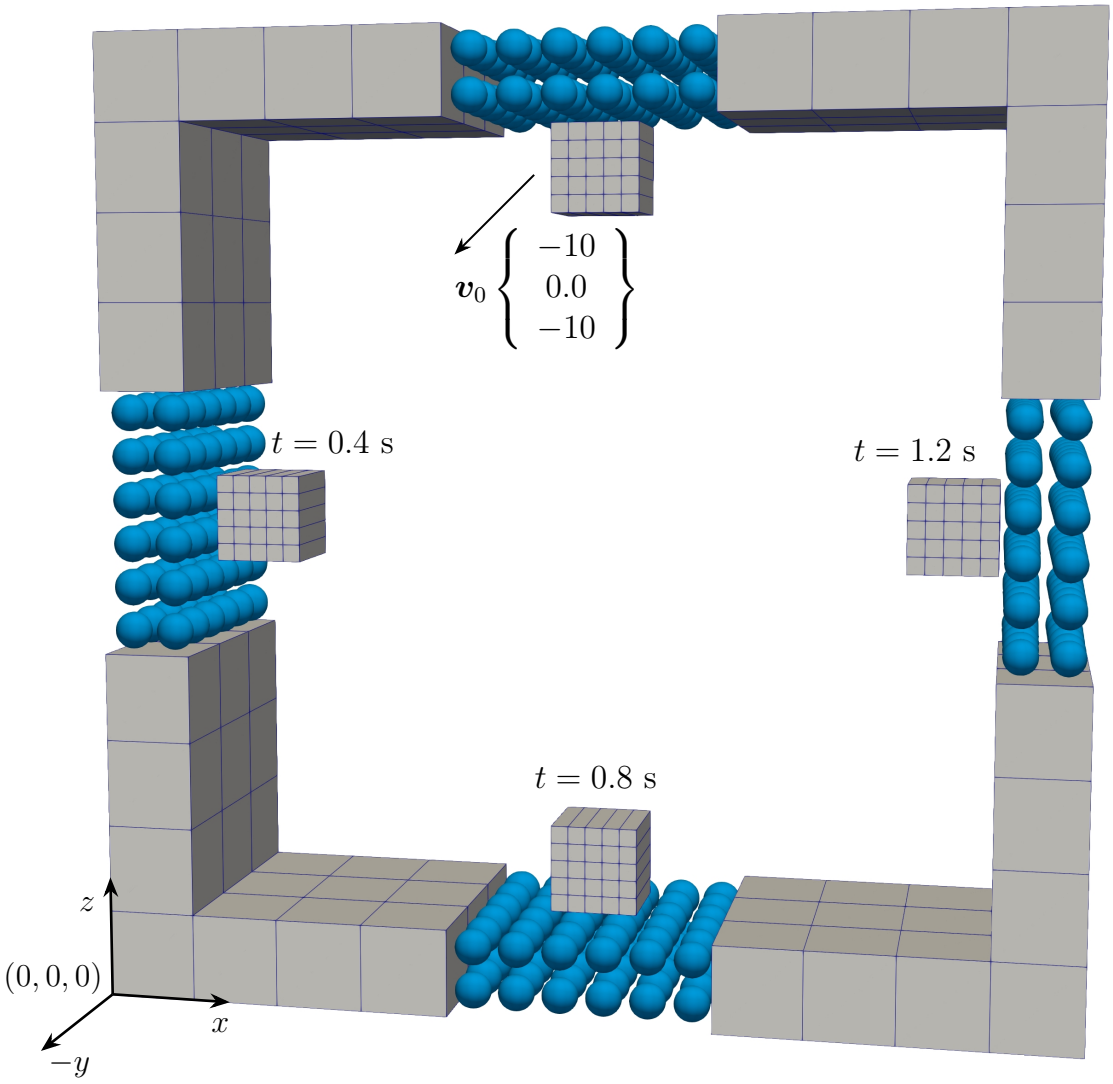

Figure 8: Contact benchmark.

The displacement and velocity plots in x-direction of the moving block are presented in Fig. 9. When the block reached the left edge of the frame at $t = 0.4$ s, Eqs. (25, 26) are satisfied and the contact bond elements become active. The block reflects and moves to hit the lower edge at $t = 0.8$ s, and,

then, it hits the right edge at $t = 1.2$ s. Note, that at $t = 0$ s, the block is close to the material points in the upper edge, and Eq. (25) is satisfied. However, because the block is moving away from the material points, Eq. (26) is not satisfied and the contact bond elements are not activated. The results validate the implementation of the contact bond element.

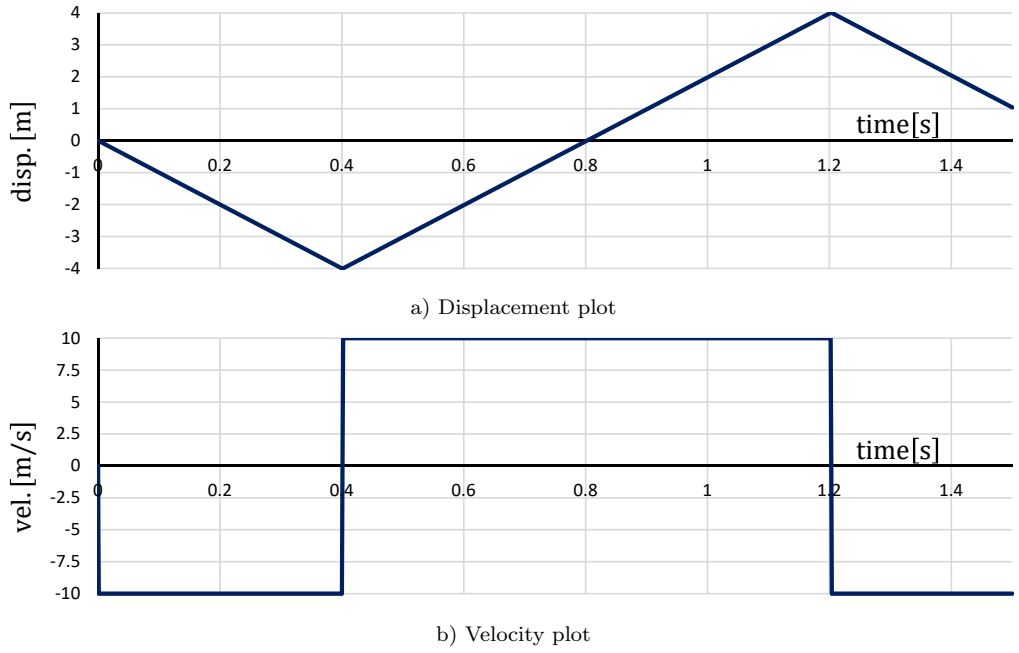

a) Displacement plot

b) Velocity plot

Figure 9: Displacement and velocity in the x-direction of the moving block.

4. Conversion of finite elements to material points

In the previous sections, the coupling of MPM with FEM and the contact of MPM with FEM have been introduced. The idea behind the coupling is to optimize the simulation by utilizing the merits of each method. As mentioned before, the FEM is more efficient and powerful than MPM as long as the elements are not highly distorted. It is possible to further optimize the simulation by starting the problem with only FEM, and during the simulation, some of the finite elements, chosen based on specified criteria, are converted to material points.

The conversion criterion is specified based on the problem being simulated. For instance, in the application of rubber-like materials, the criterion could

be the degree of element distortion measured by a certain technique. In the simulation of soil mechanics problems, the criterion could be the degree of element distortion or/and the damage percentage of finite elements based on the material model applied.

In the presented work, the criterion to convert finite elements to material points is the erosion of the finite elements by the eigenfracture approach which is applied for fracture simulation.

4.1. Eigenfracture approach

The eigenfracture approach introduced by Pandolfi and Ortiz [23] is a variational fracture model based on an energy balance between the accumulated strain energy and the fracture energy. The finite element with a strain energy larger than or equal to the fracture energy is considered to be eroded. In this approach, a finite element is either intact or eroded. The elastic energy functional of an element is given by

$$E(\boldsymbol{u}, c) = \int_{ve} \psi(\boldsymbol{F}(\boldsymbol{u}), c) dV \ , \tag{28}$$

where ve is the element volume, $\boldsymbol{F}$ is the deformation gradient, and ψ is the element elastic energy density

$$\psi(\boldsymbol{F}(\boldsymbol{u}), c) = c\ \psi^{+}(\boldsymbol{F}(\boldsymbol{u})) + \psi^{-}(\boldsymbol{F}(\boldsymbol{u})), \tag{29}$$

where ψ^{+} is the crack driving energy, which represents the part of the elastic energy responsible of the crack propagation, and ψ^{-} is the remainder part of the elastic energy

$$\psi^{-}(\boldsymbol{F}(\boldsymbol{u})) = \psi(\boldsymbol{F}(\boldsymbol{u})) - \psi^{+}(\boldsymbol{F}(\boldsymbol{u})), \tag{30}$$

and c is a binary numerical parameter

$$\begin{aligned} c &= 0, \quad \text{eroded}, \\ c &= 1, \quad \text{intact}. \end{aligned} \tag{31}$$

A finite element is eroded if

$$\int_{ve} \psi^{+}(\boldsymbol{F}(\boldsymbol{u})) dV \geq G_c |C| \ , \tag{32}$$

where G_c is the critical energy release rate, and $|C|$ is the area of the crack. The energy is divided into two parts, ψ^{+} and ψ^{-}, as shown in Eq. (29).

Various split models have been developed to specify ψ^+ and ψ^- in order to accurately depict crack development and to describe the material behavior in the presence of a crack. These split models include the volumetric-deviatoric split (VD-split) [1, 12, 16], which separates the strain tensor into volumetric and deviatoric components, the spectral-split (or TC-split) [21], which classifies the strain tensor based on the signs of the strain eigenvalues, and the Representative Crack Element (RCE) [33, 35, 34], which represents the crack as discrete crack elements. It has been shown in [8] that the RCE split model shows superior behavior compared to the TC and VD split models. For more details the reader could refer to [8, 24, 25, 28, 31, 32].

It is worth mentioning that, in order to maintain stability in numerical simulations, zero stiffness is typically avoided. Consequently, the binary numerical parameter c, as defined in Eq. (31), is often assigned a very small value rather than being set to 0 for eroded material cases. Moreover, the use of split models can result in varying stiffness behaviors for eroded materials, depending on the specific split model employed and the applied loading conditions. For example, when an eroded material is subjected to compression loading, it exhibits normal stiffness without experiencing any degradation. Furthermore, in dynamic simulations, the contribution of the inertial term helps to maintain numerical stability.

As mentioned before, the simulation starts with only finite elements. During the simulation, once a finite element becomes eroded, it converts into material points. The material points are assigned all the necessary data to replace the finite element and continue the simulation. Fig. 10 shows an eroded finite element converted into material points. The number of material points per element can be chosen freely, and the data are assigned to the material points through the shape functions provided with the local coordinates of the material points.

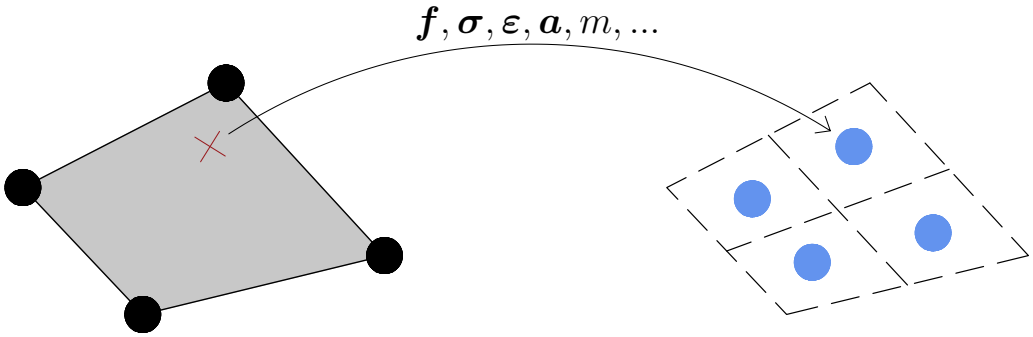

Figure 10: Conversion of FE to MPs.

An illustrative example is shown in Fig. 11. A notched specimen is fixed at the bottom and subjected to prescribed displacement in the vertical direction at the top. The initial configuration discretized initially by finite elements is depicted in Fig. 11a. In Fig. 11b, the eroded finite elements are shown (in red) just before they have been converted into material points. The created material points are presented in Fig. 11c, and the computational mesh with the activated elements is depicted in Fig. 11d. The computational mesh needs only to be created, where a potential is present having material points during the simulation. This will also reduce computational time and the required memory.

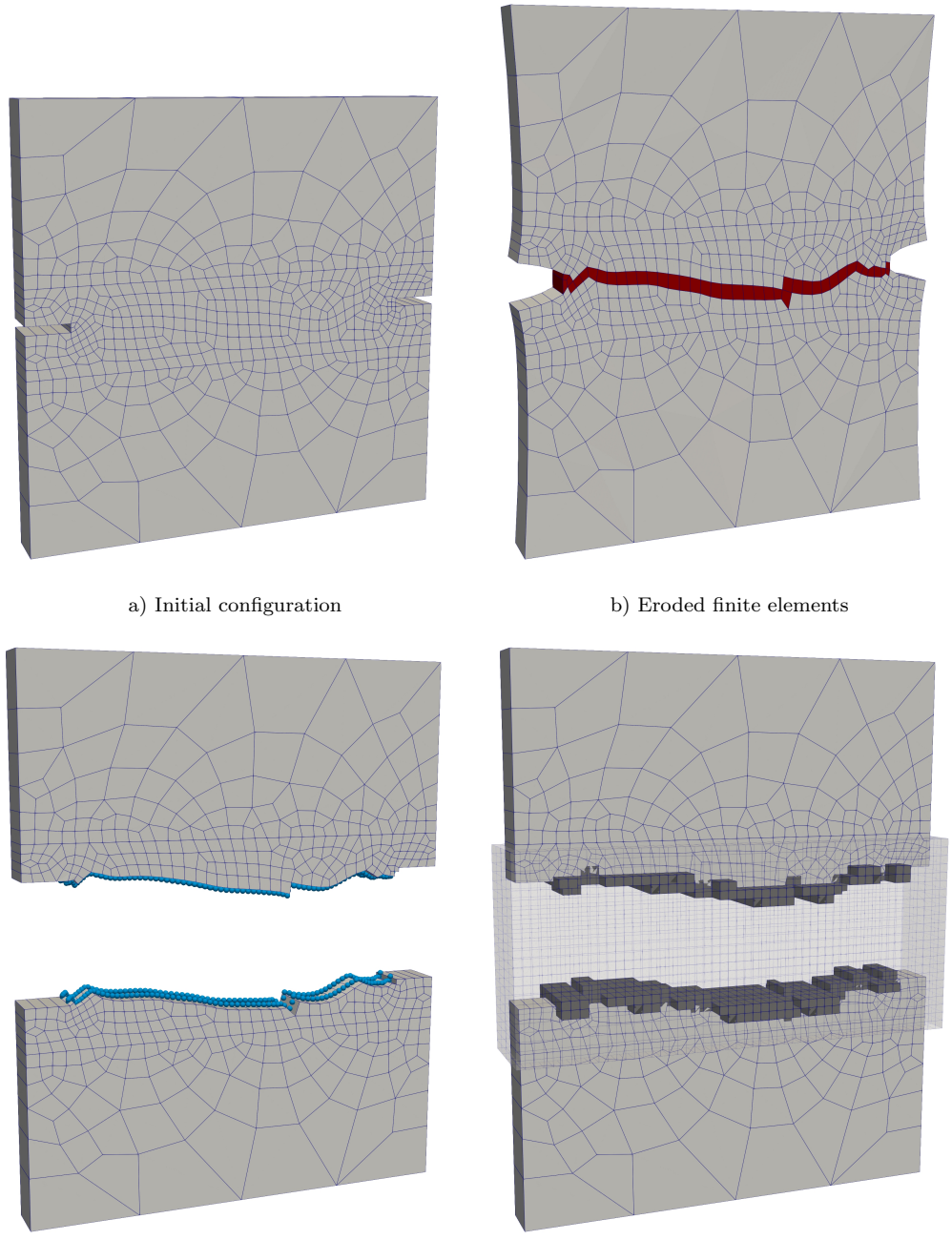

a) Initial configuration

b) Eroded finite elements

c) Material points

d) Activated elements

Figure 11: Automated conversion of eroded finite elements to material points.

5. Numerical examples

In this section, numerical examples are presented. The first example studies a body initially discretized by material points and finite elements, and the other examples depict the automated conversion of finite elements into material points. The first example is a benchmark to show the stress propagation at the interface between the material points and the finite elements. The second example is an L-shaped panel simulated in the quasi-static case. A crack branching in the dynamic case is presented in the third example. In the forth problem, a three-dimensional plate under impact is investigated. All the algorithms proposed in this work are implemented in the in-house MP-FE code written in Fortran.

5.1. Benchmark - Stress wave propagation

Stress wave propagation through the interface between the material points and the finite elements is investigated in a two-dimensional rectangular bar. The bar dimensions are 150 $\times$ 50 mm subjected to a dynamic loading of $\sigma_0 = 50$ MPa at the left edge with the amplitude function described in Fig. 12. The applied loading is then calculated as $\sigma(t) = \sigma_0 \cdot f(t)$. The bar has Young's modulus of 40 GPa, zero Poisson's ratio, and mass density of 2400 kg/m^3. The simulation is conducted with a time step of 0.5 μs. Three simulations are conducted in order to study the influence of different element sizes of MPM and FEM. The element size of the computational mesh of the MPM is kept 1.25 $\times$ 5 mm in the three simulations. Initially, 600 elements are activated with 3 $\times$ 3 material points per element. The total number of material points is 5400.

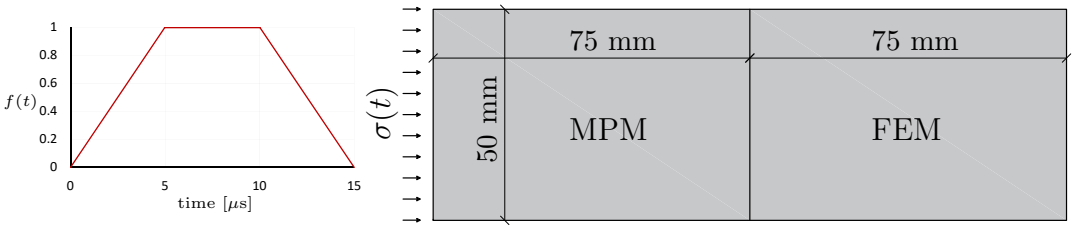

Figure 12: Bar subjected to impact loading discretized by both MPM and FEM.

In the first simulation, the element size of the computational mesh in the MPM is equal to the element size of the finite elements. As shown in Fig. 13,

the stress wave propagates smoothly through the interface, where the nodal bond elements are applied without any intermediate bond elements. Nodal bond elements are presented by the blue dots in the figure.

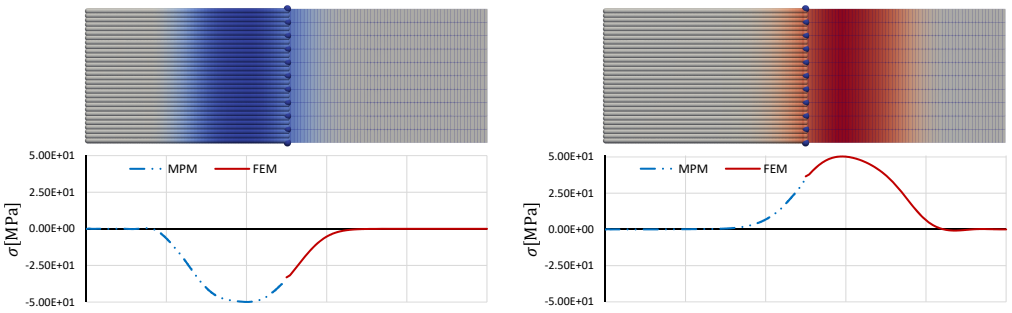

a) $t = 22$ μs b) $t = 59$ μs

Figure 13: MPM and FEM with same element size.

In the second simulation, the same problem is addressed but with a larger finite elements size of 1.25×16.7 mm as shown in Fig. 14. The results show that the stress wave is unable to propagate correctly and it becomes distorted once it reaches the nodal bond elements at the interface.

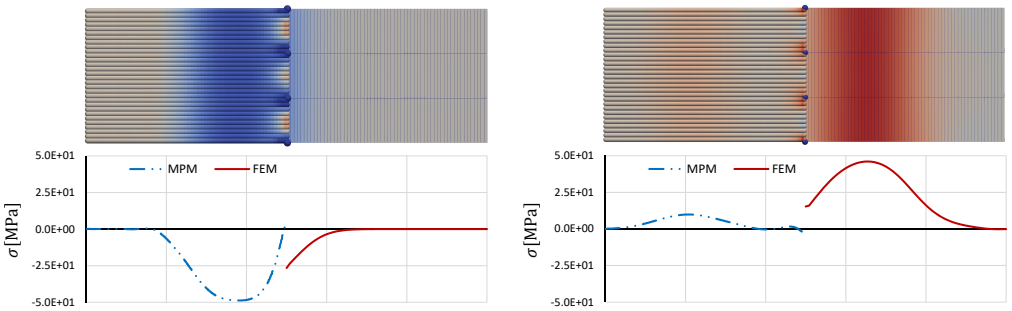

a) $t = 22$ μs b) $t = 59$ μs

Figure 14: Coarse finite element mesh with no intermediate bond elements.

The same simulation is repeated, but this time including intermediate bond elements as depicted in Fig. 15. Intermediate bond elements are presented by the red dots in the figure. By including the intermediate bond elements, the stress wave propagates correctly in the same way as in the first simulation, where the size of the elements in both MPM and FEM are the same as the plots show in both simulations.

It can be concluded from this example that if the finite element size is bigger than the element size of the computational mesh of the MPM, intermediate bond elements are required.

Furthermore, the bar is modeled using only FEM. The results obtained from the first and the third examples are compared to the results of the simulation using only FEM. The comparison is shown in Fig. 16. As the figure shows, all results, in tension and compression are in very good agreement. The comparison validates the coupling method as it shows correct stress wave propagation, when enough bond elements are provided.

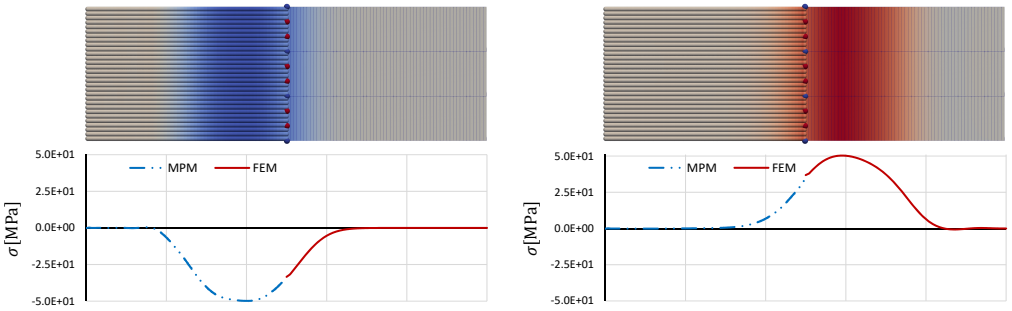

a) $t = 22\ \mu s$ b) $t = 59\ \mu s$

Figure 15: Course finite element mesh with intermediate bond elements.

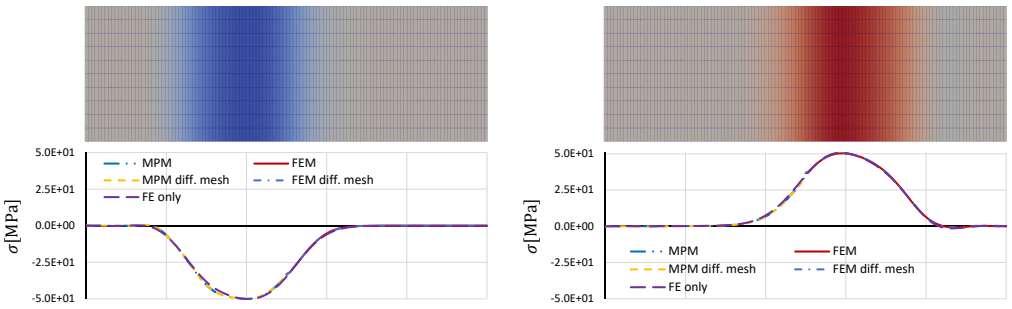

a) $t = 22\ \mu s$ b) $t = 59\ \mu s$

Figure 16: Comparison of the results obtained from different simulations.

Finally, the convergence of the proposed coupling method towards an analytical solution is investigated. For this purpose, the bar subjected to impact loading is considered, while the right edge is fixed, as described in

Fig. 17. The variation of the total reaction force as the element size changes is studied. Based on the theory of wave propagation [20], the transmitted stress, σ_T, to the fixed boundary is twice the incident stress, σ_I, which hits the boundary. As mentioned above, and shown in Fig. 13, the incident stress has an amplitude of 50 MPa. Therefore the transmitted stress amplitude must be 100 MPa. Five meshes, with square element of sizes 1/40, 1/80, 1/120, 1/160, and 1/200 m are investigated. The same mesh refinement is used for both MPM and FEM. Furthermore, for each case, 2×2 and 3×3 material points per element are addressed. Fig. 18 presents the convergence behavior in terms of the normalized stress, σ_I/σ_T, against 1/element size. As shown in the figure, convergence is achieved as the element size decreases. The number of material points has almost no influence on the result compared to the element size. The result validates the proposed coupled MPM-FEM approach.

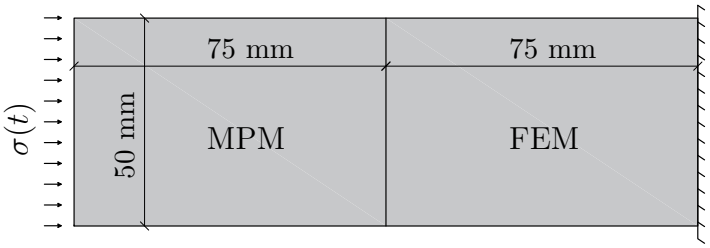

Figure 17: Fixed bar subjected to impact loading.

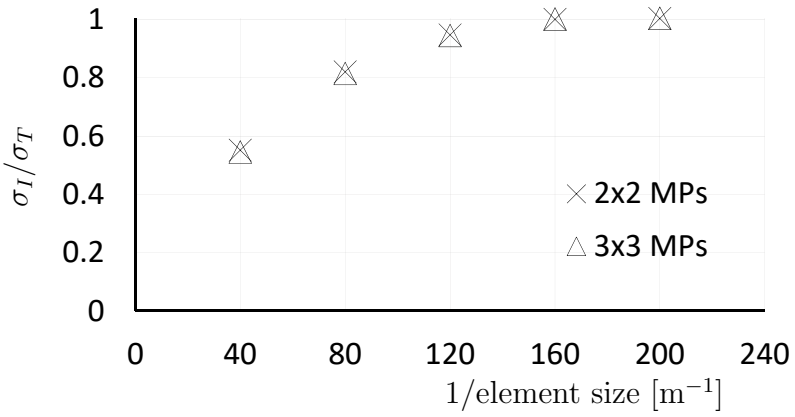

Figure 18: Convergence behavior with mesh and material point refinement.

5.2. L-shaped panel

An L-shaped specimen fixed at the bottom and subjected to prescribed displacements in quasi-static case is simulated. The geometry and the boundary conditions are described in Fig. 19a, and the finite element mesh , as well as the MPM computational grid, are shown in Fig. 19b. The element size of the computational mesh is 2.5×2.5 mm while the FE mesh is nonuniform. The material is described by Young's modulus $E = 25850$ MPa, and Poisson's ratio $\nu = 0.18$, and is subjected to prescribed displacements of 25 mm assigned to the node located at 30 mm from the edge. The displacement is divided into 1000 loading increments. The critical energy release rate is $G_c = 0.035$ N/mm.

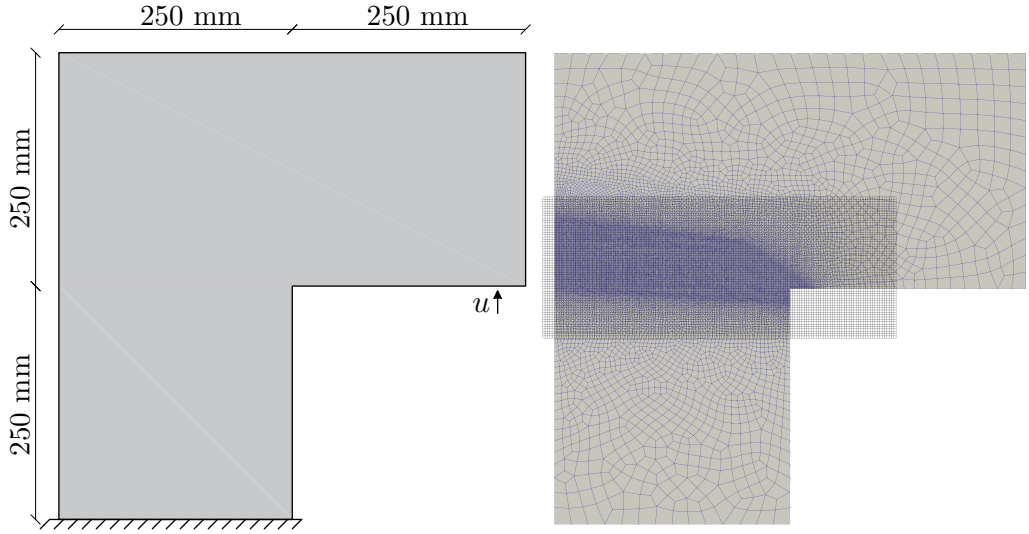

a) L-shaped geometry b) L-shaped mesh

Figure 19: L-shaped specimen.

Fig. 21 describes the crack propagation, and it shows the material points replacing the eroded finite elements during the simulation. The obtained crack pattern is in a good agreement with the experimental result documented in [38] and the numerical simulation in [15, 29, 41]. Furthermore, the total reaction force in the vertical direction is plotted in Fig. 20 and compared to other results from the literature [41, 42]. The plot of the reaction force is comparable to the results of other numerical simulations.

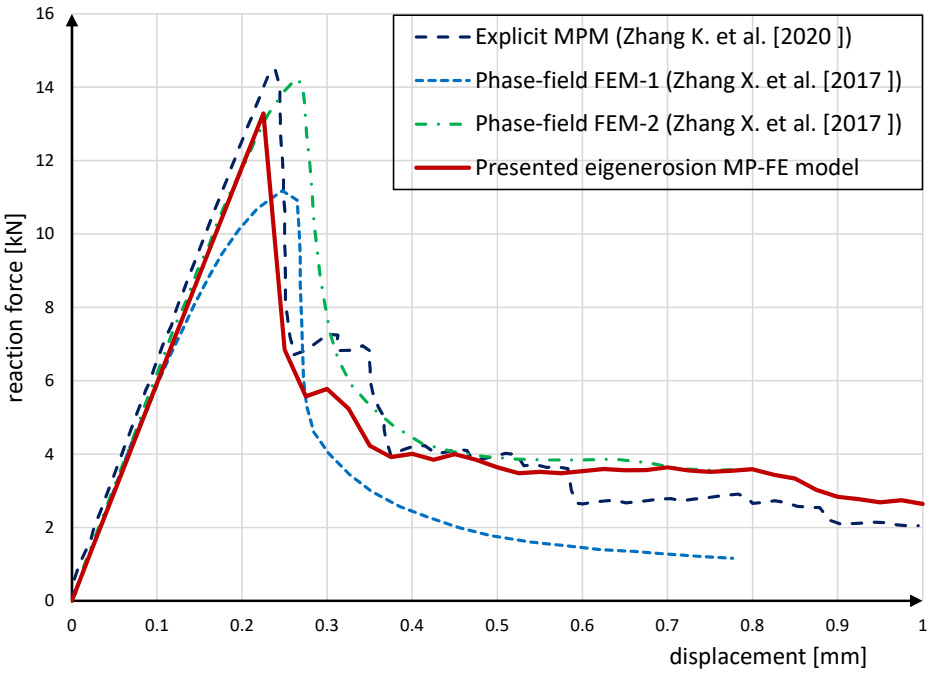

Figure 20: L-shaped specimen load-displacement curves.

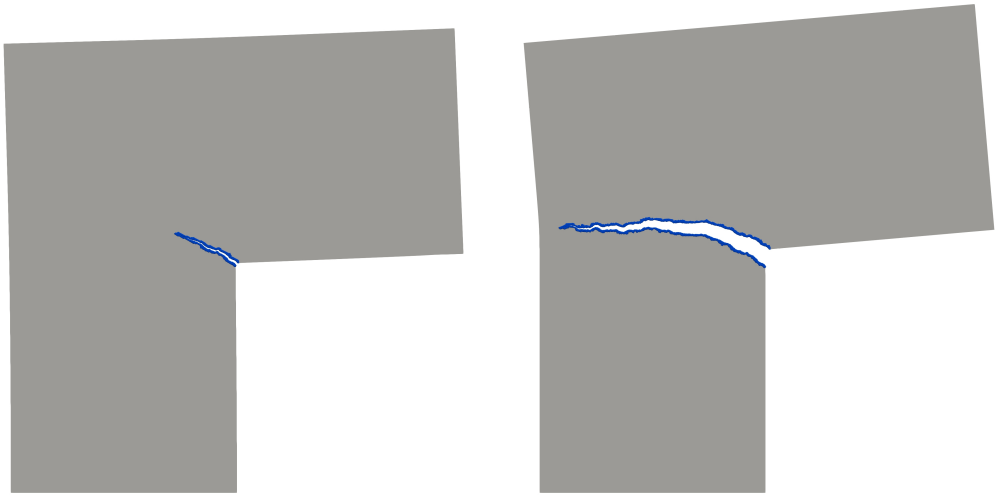

a) L-shaped panel at crack initiation

b) L-shaped panel with full crack

Figure 21: L-shaped panel crack development. Eroded finite elements are converted to material points. Material points are shown in blue. Scale factor = 10.

Fig. 22 shows a zoomed-in view of Fig. 21a. The material points are created during the simulation and replace the eroded finite elements which, are excluded from the simulation. Bond elements are also presented. They are created during the simulation at the interface between the material points and the intact finite elements. In addition to the nodal bond elements, one intermediate bond element for each continuum element is created.
The initial and the final number of finite elements are 28958 and 27449, respectively, and the final number of material points is 6036 with 4 material points per element.

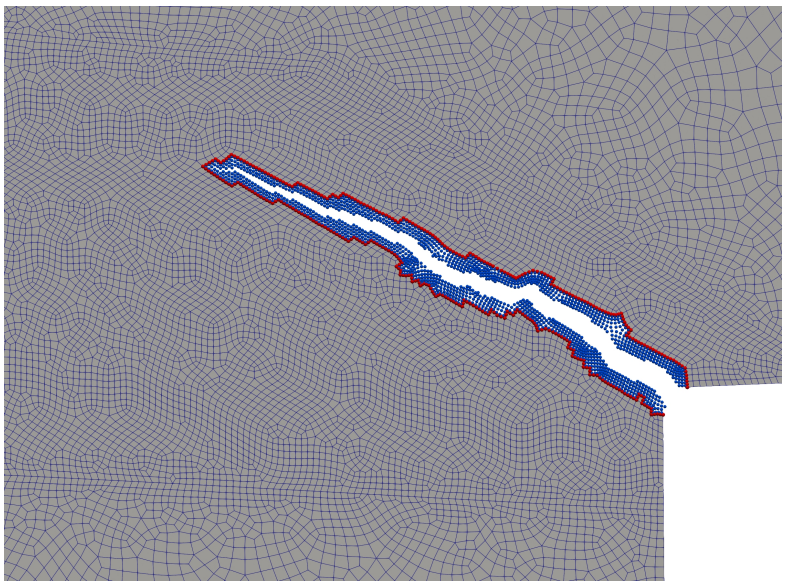

Figure 22: Conversion of eroded finite elements into material points. Material points (blue color) are connected to intact finite elements through bond elements (red color). Scale factor = 10.

5.3. Crack branching

A precracked rectangular specimen subjected to uniform stress in the dynamic case is addressed to investigate the crack branching phenomenon. The specimen is a 100×40 mm^2 plate with an initial crack of length 50 mm, as described in Fig. 23a. The material is described by mass density $\rho = 2450$ kg/m^3, Young's modulus $E = 32$ GPa, and Poisson's ratio $\nu = 0.2$, and is subjected to uniform stress of 1 MPa on both top and bottom sides, which is applied by a step function time history. The critical energy release rate is

$G_c = 1$ N/m. The time step $\Delta t = 5\ \mu s$ is chosen, and the Newmark method with parameters $\beta = 0.25$ and $\gamma = 0.5$ is used for time integration. The finite element mesh, with element size of 0.25×0.25 mm, is presented in Fig. 23b. The computational MPM mesh covers the right half of the domain, where the crack is expected to develop, with element size 0.25×0.25 mm.

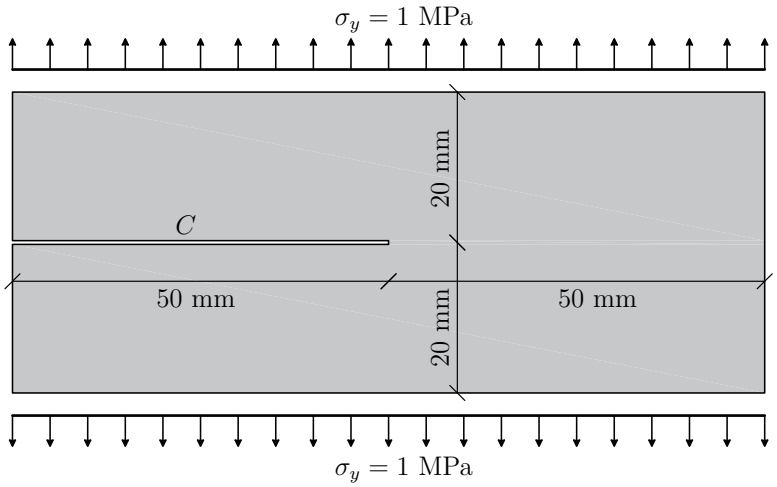

a) Model geometry and boundary conditions

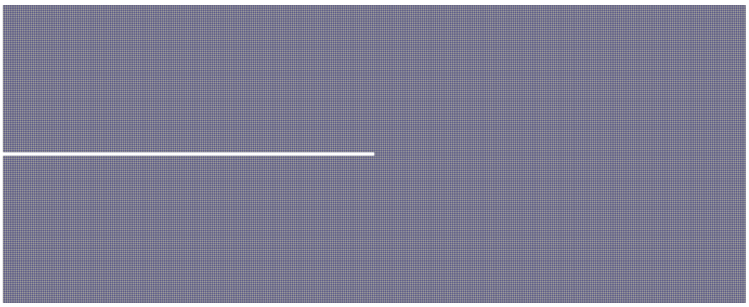

b) Finite element mesh

Figure 23: 2D dynamic crack branching model.

As depicted in Fig. 24, a crack starts at the tip of the initial notch and propagates in a straight path till it reaches a point, where two branches start to develop. The two branches then propagate till the end of the specimen. The obtained result is similar to the simulation presented in [8, 30, 31].

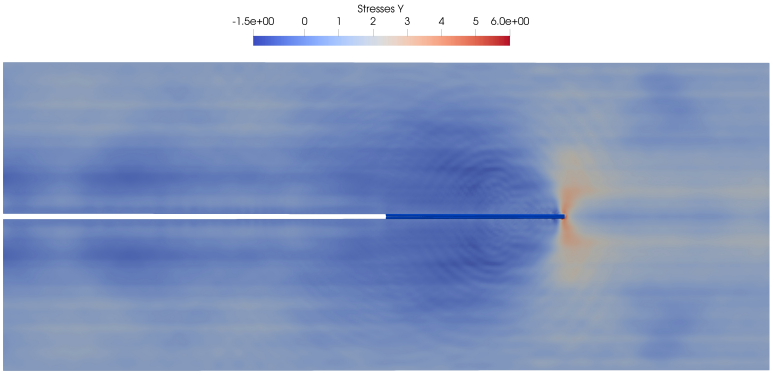

a) Crack initiation

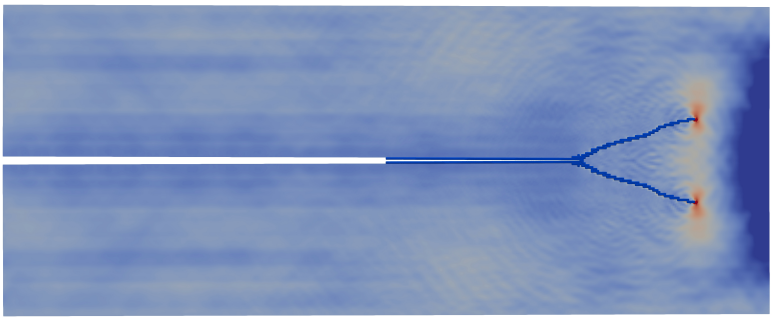

b) Crack branching

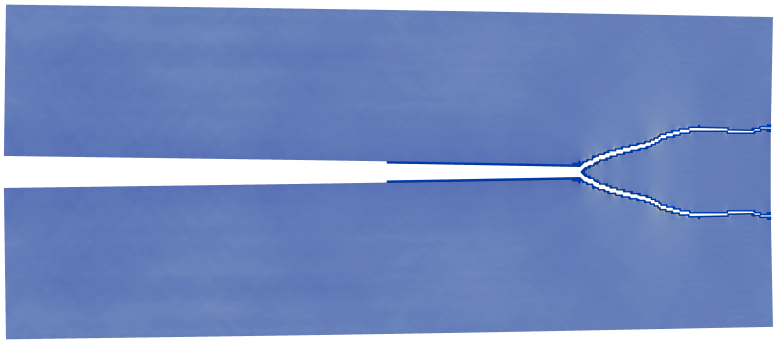

c) Final Cracking

Figure 24: Crack initiation and branching. Material points are shown in blue. Scale factor = 10.

Similar to the previous example, the details of the coupling of the material points and the intact finite elements are presented. Fig. 25 shows the

details at the crack branching spot. One intermediate bond element per each continuum element is applied.
The initial and the final number of finite elements are 63600 and 63106, respectively, and the final number of material points is 1976 with 4 material points per element.

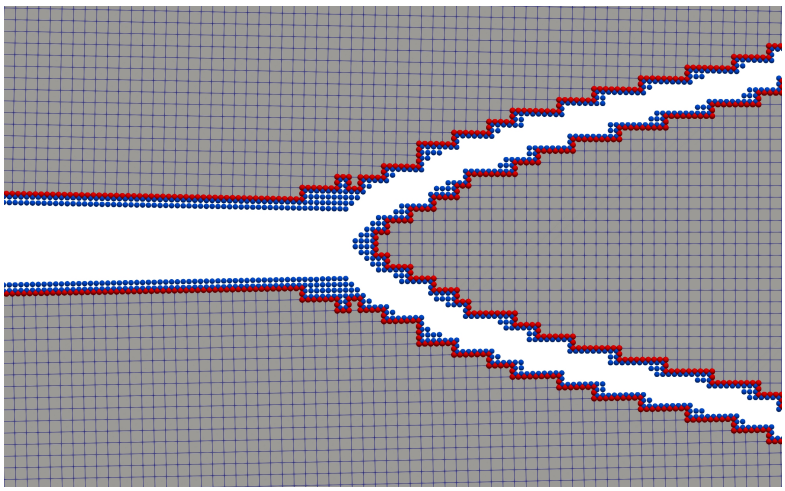

Figure 25: Eroded finite elements replaced by material points. Scale factor = 10.

5.4. Plate under impact

The final numerical example is a plate subjected to impact loading. The plate dimensions are 300 × 300 × 25 mm. Fixed supports are provided along the outer edge of the plate. The impactor is a cylinder with diameter of 50 mm and length of 100 mm. The geometry and boundary conditions are described in Fig. 26a and the finite element mesh is shown in Fig. 26b. The plate is described by mass density $\rho = 2400$ kg/m^3, Young's modulus $E = 30$ GPa, and Poisson's ratio $\nu = 0.2$. The critical energy release rate is $G_c = 0.01$ N/mm. The impactor is characterized by mass density $\rho = 7850$ kg/m^3, Young's modulus $E = 200$ GPa, and Poisson's ratio $\nu = 0.3$. The time step $\Delta t = 1$ μs is chosen, and the Newmark method with parameters $\beta = 0.5$ and $\gamma = 0.5$ is used for time integration. The impactor hits the plate at velocity of 24 m/s in vertical direction. Due to the symmetry, a quarter of the plate has been simulated. The MPM computational mesh covers the whole domain of the motion with element size equals the finite element size which is 5×5×5 mm.

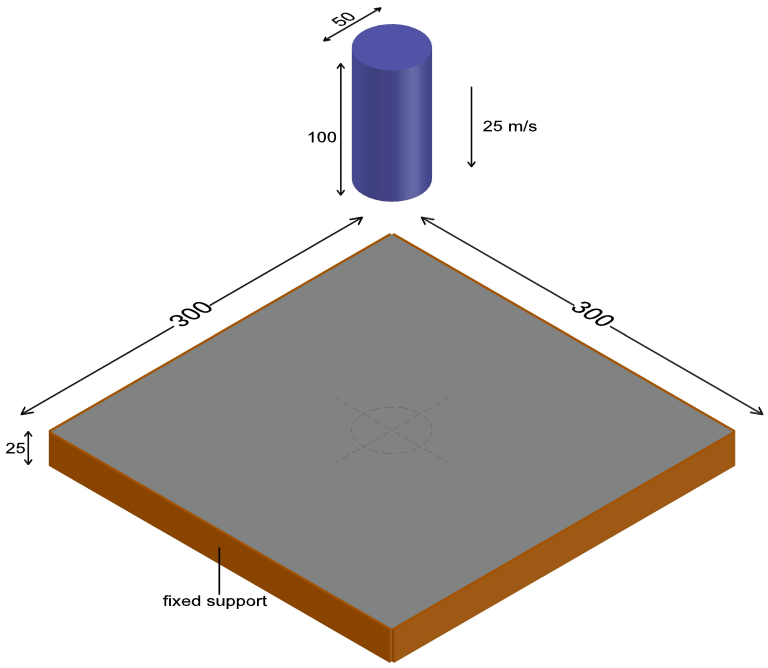

a) Plate geometry

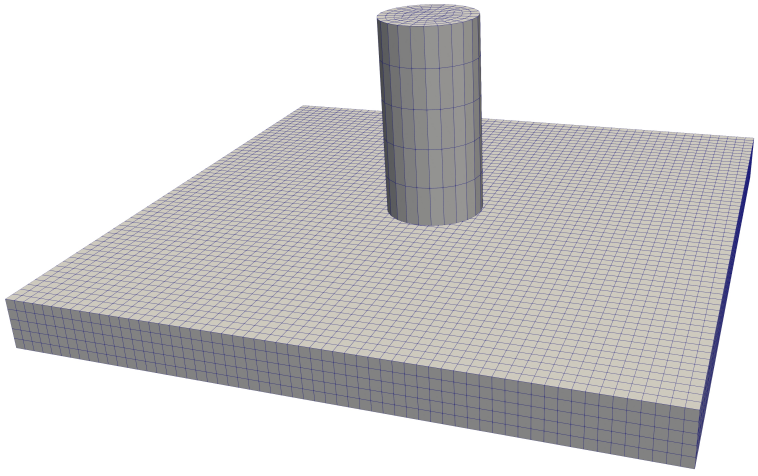

b) Finite element mesh

Figure 26: Plate under impact.

The penetration of the impactor through the plate is depicted in Fig. 28. Fig. 28a shows the top surface and Fig. 28b shows the bottom one.

The material points are indicated in blue. In Fig. 27, the evolution of the impactor's velocity and acceleration are plotted. The impactor starts moving with a constant velocity until it hits the plate. Then, acceleration in the opposite direction of the motion of the impactor is developed, and the velocity starts to decrease. After the cracking phase, the impactor starts moving in a constant velocity again, with acceleration tending to zero.

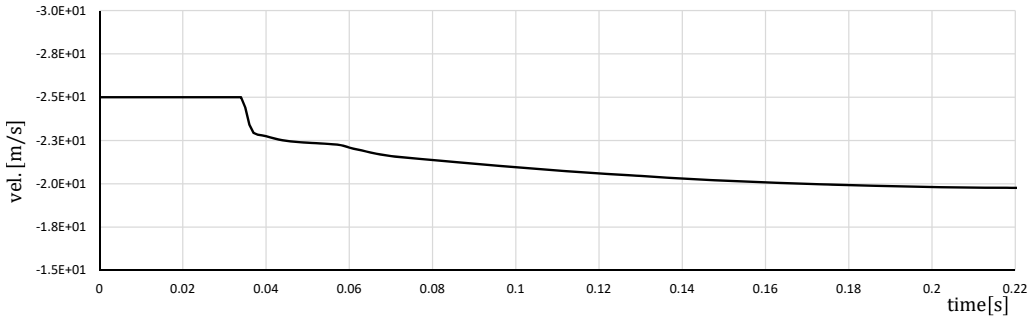

a) Impactor velocity

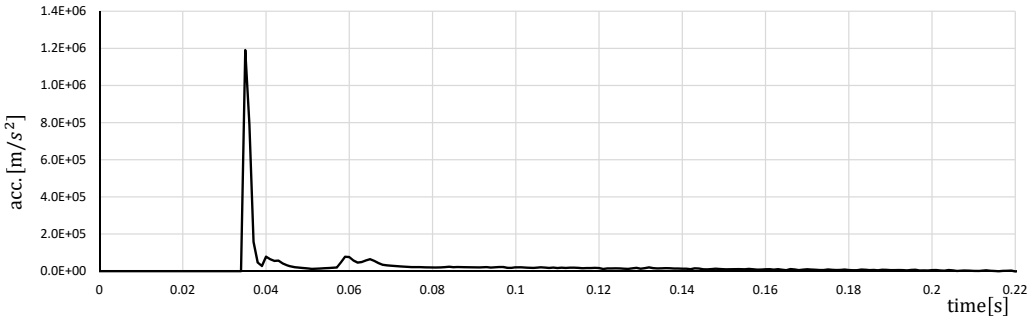

b) Impactor acceleration

Figure 27: Evolution of impactor's velocity and acceleration.

The created bond elements during the simulation are depicted in Fig. 29. In total, sixteen bond elements are created per surface of continuum finite elements, four nodal bond elements, and twelve intermediate bond elements. The initial and the final number of finite elements are 4635 and 4240, respectively, and the final number of material points is 3160 with 8 material points per element.

This example shows in a clear way the capability of the introduced approach as penetration is not possible in the standard finite element method. It also

avoids using the MPM in the far field, where the deformation is small and the finite elements are not distorted.

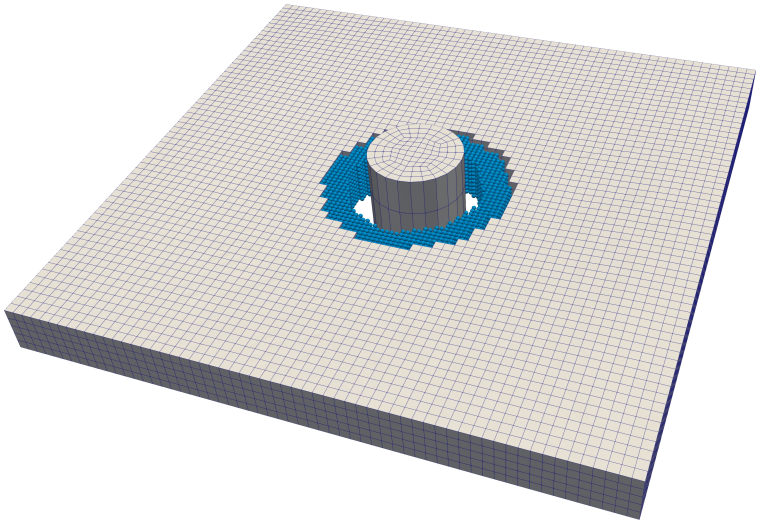

a) Top face

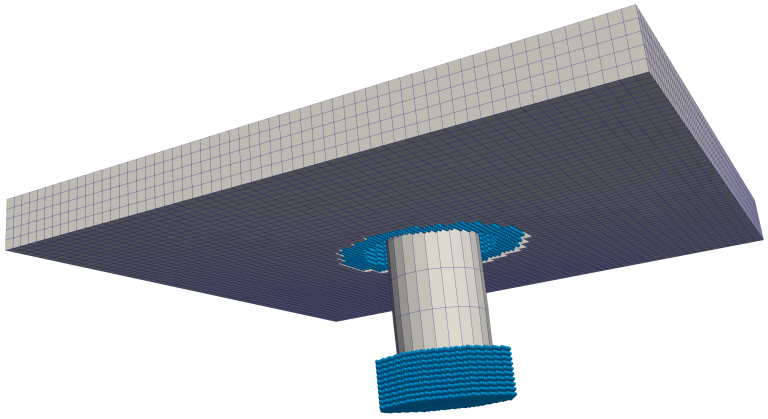

b) Bottom face

Figure 28: Plate penetrated by the impactor.

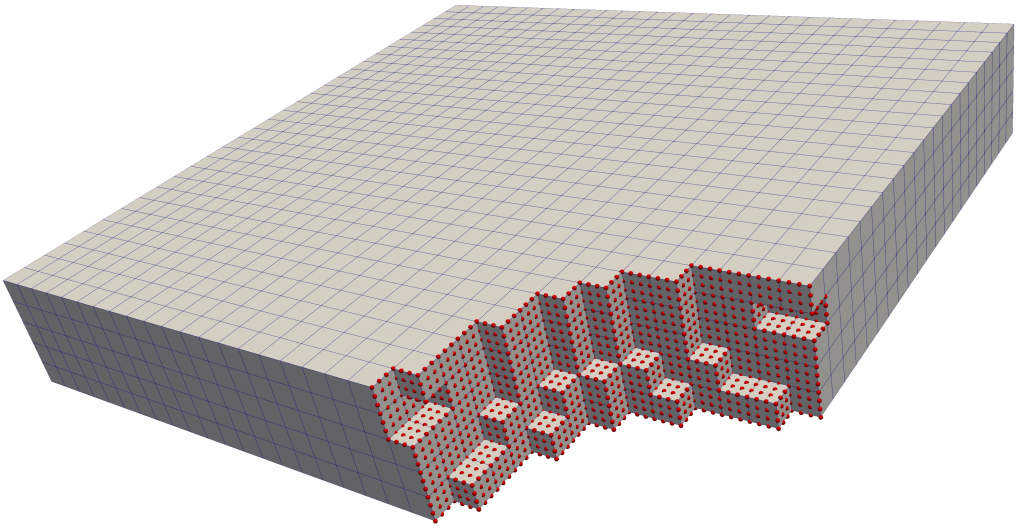

Figure 29: Formation of bond elements during plate simulation.

6. Conclusions

A novel coupling approach between MPM and FEM has been introduced. The coupling is monolithic and the system is assembled in the same way as in the standard FEM. Three types of elements are contributing to the system, the activated element of the MPM, the continuum finite element, and the bond element which connects the material points to the finite elements. The system is solved simultaneously.

The bond elements are created on the interface between the finite elements and the material points. They bond the finite elements to the activated elements in the computational mesh of the MPM. The bond is achieved using the penalty approach. The assigned large stiffness by the penalty terms prevents slip between the finite elements and the activated elements.

The bond elements are introduced at the finite elements nodes located at the interface, and additional intermediate bond elements are used on the surface of the finite elements to maintain the connectivity between the material points and the finite elements, especially when the coupling is applied for MPM and FEM with different element size.

The contact problem between MPM and FEM is also addressed in this work. It is controlled by additional two conditions to activate the bond elements. The first one, if the finite elements are close enough to the material points, and, the second, if the two bodies are approaching and not separating. If

the two conditions are satisfied, the bond elements at the interface become active and prevent any penetration of the bodies.
Trying to reach an optimum simulation, an automated conversion of finite elements to material points is presented. Starting the simulation with FEM only and during the simulation the conversion is just applied on the eroded finite elements. The eroded elements are defined by the eigenfracture approach, which models crack propagation. This approach describes a crack as a set of eroded finite elements. This property is used as a criterion to control the conversion of finite elements to material points.
Numerical examples are investigated to illustrate the capability of the developed approach.

Acknowledgment

The presented work is funded by the German Research Foundation (DFG) within Research Training Group GRK 2250/2 *"Mineral bonded composites for enhanced structural safety"*, Sub-project B4 . This financial support is gratefully acknowledged.

References

[1] Amor, H.; Marigo, J.-J.; and Maurini, C.; (2009). Regularized formulation of the variational brittle fracture with unilateral contact: Numerical experiments. *Journal of the Mechanics and Physics of Solids*, 57:1209–1229.

[2] Aulisa, E.; and Capodaglio, G.; (2019). Monolithic coupling of the implicit material point method with the finite element method. *Computers and Structures*, 219:1–15.

[3] Bardenhagen, S.; and Kober, E.; (2004). The generalized interpolation material point method. *Computer Modeling in Engineering and Sciences*, 5:477–496.

[4] Bathe, K.-J.; (2006). *Finite element procedures*. Englewood Cliffs: Prentice Hall.

[5] Charlton, T.; Coombs, W.; and Augarde, C.; (2017). iGIMP: An implicit generalised interpolation material point method for large deformations. *Computers and Structures*, 190:108–125.

[6] Chen, Z.; Qiu, X.; Zhang, X.; and Lian, Y.; (2015). Improved coupling of finite element method with material point method based on a particle-to-surface contact algorithm. *Computer Methods in Applied Mechanics and Engineering*, 293:1–19.

[7] Chihadeh, A.; and Kaliske, M.; (2022). A coupled implicit material point-finite element method for modeling reinforced materials. *Engineering Computations*, 39:2553–2580.

[8] Chihadeh, A.; Storm, J.; and Kaliske, M.; (2023). Fracture modeling by the eigenfracture approach for the implicit material point method framework. *International Journal for Numerical Methods in Engineering*, 124:1280–1306.

[9] Coombs, W.; Augarde, C.; Brennan, A.; Brown, M.; Charlton, T.; Knappett, J.; Motlagh, Y.; and Wang, L.; (2020). On lagrangian mechanics and the implicit material point method for large deformation elasto-plasticity. *Computer Methods in Applied Mechanics and Engineering*, 358:112622.

[10] De Borst, R.; Crisfield, M.; Remmers, J.; and Verhoosel, C.; (2012). *Nonlinear Finite Element Analysis of Solids and Structures*. Wiley, Chichester.

[11] Dhakal, T. R.; and Zhang, D. Z.; (2016). Material point methods applied to one-dimensional shock waves and dual domain material point method with sub-points. *Journal of Computational Physics*, 325:301–313.

[12] Freddi, F.; and Royer-Carfagni, G.; (2010). Regularized variational theories of fracture: a unified approach. *Journal of the Mechanics and Physics of Solids*, 58:1154–1174.

[13] Gan, Y.; Sun, Z.; Chen, Z.; Zhang, X.; and Liu, Y.; (2018). Enhancement of the material point method using b-spline basis functions. *International Journal for numerical methods in engineering*, 113:411–431.

[14] Guilkey, J.; and Weiss, J.; (2003). Implicit time integration for the material point method: Quantitative and algorithmic comparisons with the finite element method. *International Journal for Numerical Methods in Engineering*, 57:1323–1338.

[15] Kakouris, E.; and Triantafyllou, S. P.; (2017). Phase-field material point method for brittle fracture. *International Journal for Numerical Methods in Engineering*, 112:1750–1776.

[16] Lancioni, G.; and Royer-Carfagni, G.; (2009). The variational approach to fracture mechanics. a practical application to the french panthéon in paris. *Journal of Elasticity*, 95:1–30.

[17] Lian, Y.; Zhang, X.; and Liu, Y.; (2011). Coupling of finite element method with material point method by local multi-mesh contact method. *Computer Methods in Applied Mechanics and Engineering*, 200:3482–3494.

[18] Lian, Y.; Zhang, X.; and Liu, Y.; (2012). An adaptive finite element material point method and its application in extreme deformation problems. *Computer Methods in Applied Mechanics and Engineering*, 241:275–285.

[19] Long, C.; Zhang, D.; Bronkhorst, C.; and Gray III, G.; (2016). Representing ductile damage with the dual domain material point method. *Computer Methods in Applied Mechanics and Engineering*, 300:611–627.

[20] Meyers, M. A.; (1994). *Dynamic behavior of materials*. John wiley & sons.

[21] Miehe, C.; Welschinger, F.; and Hofacker, M.; (2010). Thermodynamically consistent phase-field models of fracture: Variational principles and multi-field fe implementations. *International Journal for Numerical Methods in Engineering*, 83:1273–1311.

[22] Nguyen, V. P.; Nguyen, C. T.; Rabczuk, T.; and Natarajan, S.; (2017). On a family of convected particle domain interpolations in the material point method. *Finite Elements in Analysis and Design*, 126:50–64.

[23] Pandolfi, A.; and Ortiz, M.; (2012). An eigenerosion approach to brittle fracture. *International Journal for Numerical Methods in Engineering*, 92:694–714.

[24] Qinami, A.; Bryant, E. C.; Sun, W.; and Kaliske, M.; (2019). Circumventing mesh bias by r-and h-adaptive techniques for variational eigenfracture. *International Journal of Fracture*, 220:129–142.

[25] Qinami, A.; Pandolfi, A.; and Kaliske, M.; (2020). Variational eigenerosion for rate-dependent plasticity in concrete modeling at small strain. *International Journal for Numerical Methods in Engineering*, 121:1388–1409.

[26] Sadeghirad, A.; Brannon, R. M.; and Burghardt, J.; (2011). A convected particle domain interpolation technique to extend applicability of the material point method for problems involving massive deformations. *International Journal for Numerical Methods in Engineering*, 86:1435–1456.

[27] Sadeghirad, A.; Brannon, R. M.; and Guilkey, J.; (2013). Second-order convected particle domain interpolation (cpdi2) with enrichment for weak discontinuities at material interfaces. *International Journal for Numerical Methods in Engineering*, 95:928–952.

[28] Schmidt, B.; Fraternali, F.; and Ortiz, M.; (2009). Eigenfracture: an eigendeformation approach to variational fracture. *Multiscale Modeling & Simulation*, 7:1237–1266.

[29] Shahba, A.; and Ghosh, S.; (2019). Coupled phase field finite element model for crack propagation in elastic polycrystalline microstructures. *International Journal of Fracture*, 219:31–64.

[30] Steinke, C.; Özenç, K.; Chinaryan, G.; and Kaliske, M.; (2016). A comparative study of the r-adaptive material force approach and the phase-field method in dynamic fracture. *International Journal of Fracture*, 201:97–118.

[31] Stochino, F.; Qinami, A.; and Kaliske, M.; (2017). Eigenerosion for static and dynamic brittle fracture. *Engineering Fracture Mechanics*, 182:537–551.

[32] Storm, J.; Qinami, A.; and Kaliske, M.; (2021). The concept of representative crack elements applied to eigenfracture. *Mechanics Research Communications*, 116:103747.

[33] Storm, J.; Supriatna, D.; and Kaliske, M.; (2020). The concept of representative crack elements for phase-field fracture: Anisotropic elasticity and thermo-elasticity. *International Journal for Numerical Methods in Engineering*, 121:779–805.

[34] Storm, J.; Yin, B.; and Kaliske, M.; (2022a). The concept of representative crack elements (RCE) for phase-field fracture: transient thermo-mechanics. *Computational Mechanics*, p:1–12.

[35] Storm, J.; Yin, B.; and Kaliske, M.; (2022b). The concept of representative crack elements (RCE) for phase-field fracture—non-linear materials and finite deformations. *International Journal for Numerical Methods in Engineering*. (submitted).

[36] Sulsky, D.; Chen, Z.; and Schreyer, H.; (1994). A particle method for history-dependent materials. *Computer Methods in Applied Mechanics and Engineering*, 118:179–196.

[37] Tielen, R.; Wobbes, E.; Möller, M.; and Beuth, L.; (2017). A high order material point method. *Procedia Engineering*, 175:265–272.

[38] Winkler, B.; Hofstetter, G.; and Niederwanger, G.; (2001). Experimental verification of a constitutive model for concrete cracking. *Proceedings*

684 *of the Institution of Mechanical Engineers, Part L: Journal of Materials:*
685 *Design and Applications*, 215:75–86.

686 [39] Yamaguchi, Y.; Moriguchi, S.; and Terada, K.; (2021). Extended b-
687 spline-based implicit material point method. *International Journal for*
688 *Numerical Methods in Engineering*, 122:1746–1769.

689 [40] Zhang, D. Z.; Ma, X.; and Giguere, P. T.; (2011). Material point method
690 enhanced by modified gradient of shape function. *Journal of Computa-*
691 *tional Physics*, 230:6379–6398.

692 [41] Zhang, K.; Shen, S.-L.; and Zhou, A.; (2020). Dynamic brittle fracture
693 with eigenerosion enhanced material point method. *International Journal*
694 *for Numerical Methods in Engineering*, 121:3768–3794.

695 [42] Zhang, X.; Vignes, C.; Sloan, S. W.; and Sheng, D.; (2017). Numerical
696 evaluation of the phase-field model for brittle fracture with emphasis on
697 the length scale. *Computational Mechanics*, 59:737–752.

Highlights

- *A novel approach is developed to couple implicit MPM and FEM.*
- *Bond elements are created at the interface between material points and finite elements.*
- *An automated conversion of finite elements to material points for fracture simulation is introduced.*